PAPER • OPEN ACCESS

Investigation of microstructural evolution of irradiation-induced defects in tungsten: an experimental–numerical approach

To cite this article: Salahudeen Mohamed *et al* 2025 *Nucl. Fusion* **65** 066007

OPEN ACCESS
IOP Publishing | International Atomic Energy Agency
Nuclear Fusion
Nucl. Fusion **65** (2025) 066007 (28pp)
https://doi.org/10.1088/1741-4326/add027

Investigation of microstructural evolution of irradiation-induced defects in tungsten: an experimental–numerical approach

Salahudeen Mohamed[1,*], Qian Yuan[1], Dimitri Litvinov[1], Jie Gao[2,*], Ermile Gaganidze[1], Dmitry Terentyev[3], Hans-Christian Schneider[1] and Jarir Aktaa[1]

[1] Karlsruhe Institute of Technology (KIT), Institute for Applied Materials, Hermann-von-Helmholtz-Platz 1, 76344 Eggenstein-Leopoldshafen, Germany
[2] Key Laboratory of Nuclear Physics and Ion-Beam Application, Institute of Modern Physics, Fudan University, Shanghai 200433, China
[3] SCK • CEN, Institute of Nuclear Materials Science, Boeretang 200, B2400 Mol, Belgium

E-mail: Salahudeen.kunju@kit.edu and jiegao@fudan.edu.cn

Received 5 December 2024, revised 20 March 2025
Accepted for publication 24 April 2025
Published 9 May 2025

Abstract

This study employs an integrated experimental–numerical approach to assess the microstructural evolution of irradiation-induced defects in tungsten (W), which is being considered for fusion applications. A cluster dynamics (CD) model is utilized, and simulations are performed for irradiated disk-shaped compact tension W specimens. Experimental results indicate that the primary irradiation-induced defects in W at temperatures of 400 °C and 600 °C include dislocation loops ($^1/_2$<111> and <100>) and voids. Both experimental and CD results reveal that, at higher temperatures, the $^1/_2$<111> loop population surpasses that of <100> loops, primarily due to the higher formation free energy of <100> loops compared to $^1/_2$<111> loops. Given the high mobility of $^1/_2$<111> loops in W, in the absence of traps, most $^1/_2$<111> loops are absorbed by sinks or coalesce with <100> loops, leading to a reduced $^1/_2$<111> loop population, as supported by the CD model. However, the introduction of traps results in an increased $^1/_2$<111> loop population. The long-term evolution of loops demonstrates that the interaction between $^1/_2$<111> and <100> loops facilitates the transfer of self-interstitial atoms between loops with different Burgers vectors, causing shifts in the populations of both loop types. The CD model reliably predicts the irradiation-induced microstructure in neutron-irradiated W, considering loops, voids and C15 clusters, while integrating the current state-of-the-art knowledge on radiation damage evolution and W energetics.

* Authors to whom any correspondence should be addressed.

Keywords: neutron irradiation, cluster dynamics, transmission electron microscopy, defect evolution, tungsten

(Some figures may appear in colour only in the online journal)

1. Introduction

The future tokamak fusion reactors, namely the international thermo-nuclear experimental reactor (ITER) and DEMOnstration tokamak (DEMO), are installed with in-vessel components that are subjected to high fluence of 14 MeV neutrons and high heat flux loads [1, 2]. Tungsten (W) is employed as armor material in the divertor of ITER and DEMO due to its low sputtering rate, high melting temperature and high thermal conductivity [3, 4]. The hostile fusion-relevant irradiation environment in the tokamak reactor during operation leads to the formation of irradiation-induced defects in W, such as dislocation loops, voids and transmutation products, due to primary knock-on atoms (PKAs) [5, 6]. Consequently, the W material undergoes degradation due to irradiation-induced cascade damage and transmutation, which alters the thermo-physical and mechanical properties at different stages of its lifecycle during operation [7, 8]. In particular, the irradiation-induced defect formation in W leads to various issues, such as hardening, swelling and loss of ductility. Moreover, these irradiation-induced defects contribute to an increase in the ductile-to-brittle transition temperature in W [9, 10]. Due to these factors, W-based components in the tokamak are prone to failure, which consequently reduces its lifespan [11]. Therefore, efforts are required to gain some insights into the formation and evolution of the irradiation-induced dislocation loops and voids, and to utilize this information for the development of W-based components for fusion-relevant applications.

Studies have been carried out by many authors using experimental analysis to investigate the underlying mechanisms of the microstructural evolution of irradiation-induced defect features in W [12–16]. In a study carried out by Li *et al*, irradiation experiments using 30 keV He^+ were conducted on W samples to understand the evolution of dislocation loops depending on irradiation temperature, dose and thickness of the sample using *in situ* transmission electron microscopy (TEM) [15]. The study demonstrated that the pre-existing dislocation lines have a significant influence on the Burgers vector, density and size of the dislocation loops. Moreover, the role of the surface of thin foil acting as sinks influences the overall density distribution of the dislocation loops. Using TEM analysis, Klimenkov *et al* investigated W after neutron irradiation to about 1 dpa at various irradiation temperatures and observed irradiation-induced dislocation loops and voids [17]. In the experimental work carried out by Chauhan *et al* on the neutron irradiated W at about 1 dpa, coarsening of voids was observed when increasing the post-irradiation annealing temperature and time [16]. Dislocation loops and voids of size 10 nm and 10–65 nm, respectively, were examined by TEM by Durrschnabel *et al* [12] in W material irradiated at 800 °C and 1.25 dpa. The dislocation loop populations of $1/2<111>$ and $<100>$ are reported in various experimental studies [18, 19]. Only $1/2<111>$ loops were observed in W irradiated with 15–85 keV He^+ to 3 dpa at 500 °C in [20–22]. However, in some experimental studies, the coexistence of $1/2<111>$ and $<100>$ loops has been noted. The lower mobility of $<100>$ loops contributes to the irradiation hardening and embrittlement in W [15]. Molecular dynamics (MD) simulations conducted by Sand *et al* [23] on W irradiated with 150 keV W PKAs revealed that $<100>$ loops form as a result of cascade collapse. In other studies by Yi *et al* [14, 24], W samples were irradiated with 150 keV W ions at 500 °C and a dose of 1 dpa, where the majority of loops were identified as $1/2$ $<111>$ loops, with $<100>$ loops accounting for 25% in post-irradiation analyses. A higher percentage of $<100>$ loops was observed with the increasing PKA energy in experimental works by Yi *et al* [24]. In the study by English and Jenkins [25] on irradiated molybdenum, an increase in the $<100>$ loop density was reported due to the higher deposited energy density. However, according to Sand *et al*, at PKA energies above 200 keV, there is a decrease in the deposited energy density due to cascade fragmentation [26].

The irradiation of in-vessel materials is currently being conducted in surrogate fusion reactor facilities since actual fusion environment material testing facilities are not yet available. Moreover, employing only experimental testing to sort and down-select candidate materials for in-vessel components is expensive. In order to accelerate the development of fusion-relevant materials, predictive models are useful as they can emulate fusion irradiation conditions. This could aid in the reduction of costs related to conducting irradiation experiments. In particular, the irradiation damage in nuclear materials is multi-scale in nature and there is a need to understand the long-term kinetic evolution of defects. In this regard, meso-scale models like cluster dynamics (CD) and the kinetic Monte Carlo (KMC) method are usually employed to analyze the evolution of irradiation-induced defect features in W [27]. Due to constraints in the computational domain, the KMC approach can only accommodate defects of a few nanometers, while for the CD method there are no constraints when incorporating the size of the defect clusters and it can handle defects with larger cluster sizes. However, there is a need for higher computational resources in CD to perform simulations for larger defect clusters. To overcome these difficulties, various mathematical schemes have been developed to reduce the cost associated with the CD method. In the work of Zhao *et al,* CD methods have been employed to study the helium/hydrogen retention in W [28]. In the numerical analyses conducted by Li *et al* [29]

and Krasheninnikov *et al* [30], the nucleation and diffusion of helium atoms in W were analyzed in detail using the CD model. Using the spatially dependent CD method, Shah *et al* [31] analyzed the formation of helium vacancy clusters in a W monoblock and found that due to the emission of helium from the surface, a lower retention of helium clusters is observed. A similar study was conducted by Faney *et al* [32] using the spatial dependent CD method to analyze tendril formation in W exposed to helium. However, there are some limitations to the CD model. The CD model for defect cluster evolution incorporates numerous parameters, and uncertainties in these parameters can impact the reliability of simulation results. Reaction rates are influenced by various factors, such as the capture radius, mobility, composition and morphology [33]. Therefore, an extensive database of fundamental properties is required for defect clusters of different sizes. However, creating such a database poses significant challenges due to the larger size ranges [33].

The defect characteristics in neutron-irradiated W vary depending on the reactor type, even when irradiation conditions are nearly identical [17]. Additionally, defect evolution and growth are influenced not only by the neutron flux and irradiation temperature but also by the characteristics of the neutron spectrum [16]. As a result, each experimental irradiation campaign yields distinct results, contributing to a broader understanding of neutron radiation damage. This study aims to explore the formation and evolution of irradiation-induced effects in W as a function of the irradiation temperature. Specifically, it focuses on experimental data of defect densities in W irradiated at 400 °C and 600 °C, where variations in the relative population of $^1/_2$<111> and <100> loops are observed. As an initial step, a CD model for W is developed using these experimental parameters, allowing for the examination of the evolution of irradiation-induced defects at 400 °C and 600 °C. After validating the CD model against experimental data, further investigations are conducted to analyze the effects of trap elements, cascade overlap and loop reactions ($^1/_2$<111> + <100>). Additionally, this approach can be extended to study defect evolution at higher irradiation temperatures (>600 °C), which is planned as the next step in our research.

So far, based on previous computational modeling works using the CD method in W, there has been no study investigating the long-term evolution of dislocation loops and voids. In order to address this aspect, an in-house CD method is employed, which has the flexibility to integrate defect features such as dislocation loops, voids, c15 clusters and impurities as a function of the irradiation dose and temperature. The present study aims at the investigation of the microstructural evolution of irradiation-induced defects using an integrated experimental–numerical approach. Moreover, the interaction of loops of different Burgers vectors, $^1/_2$<111> and <100>, with voids, impurities and transmuted elements, and the resulting influence on the overall evolution of defect populations is studied. Dislocation loop variation due to the reaction between $^1/_2$<111> and <100> loops and trap-mediated 1D loop migration are also considered.

The paper is organized as follows: The next section describes the CD model, and section 3 reports the experimental results in comparison to those obtained using the CD-based numerical simulations. Relevant discussions and conclusions are reported in sections 4 and 5, respectively.

2. Model description

2.1. CD model

The CD method is a mathematical model based on a rate theory approach to mimic and study the kinetics of the microstructural evolution of defects in materials [29, 34, 35]. It provides insights on the mechanisms involved in the radiation damage, which can be employed to analyze nucleation of dislocation loops, void formation, precipitation and several other irradiation-induced phenomena, such as swelling [36]. In the CD method/simulation, the microstructural evolution of the system is described by means of a system of differential equations on the concentration of the cluster. It computes the temporal evolution of the cluster size and concentration based on the kinetic reaction of irradiation-induced defects considered in the system. The evolution of the cluster concentration of irradiation-induced defects is represented by the following equation:

$$\frac{\mathrm{d}C(y)}{\mathrm{d}t} = G_{V,I} - L^{y}_{\mathrm{sink}} - \sum_{x} k^{x}_{y} C(y)\, C(x) - \sum_{x} g^{x}_{y} C(y) + \sum_{x} k^{x}_{y'} C(y')\, C(x) + \sum_{x} g^{x}_{y''} C(y'') \tag{1}$$

where $G_{V,I}$ denotes the defect production rate. $C(x)$ and $C(y)$ represent the concentration of defects of types x and y, respectively, and L^{y}_{sink} signifies the loss rate of the defects through sinks (surface, dislocation lines, grain boundaries). The interactions among the irradiation-induced defects are defined in terms of the reaction coefficients (k^{x}_{y}, g^{x}_{y}, $k^{x}_{y'}$ and $g^{x}_{y''}$). k^{x}_{y} describes the rate of defect y absorbing defect x, while g^{x}_{y} represents the rate of defect y emitting the mobile defect x. $k^{x}_{y'}$ denotes the generation of defect y due to the reaction between defects y' and x. $g^{x}_{y''}$ depicts the emission of defect x by defect y''.

As a result of neutron irradiation, cascade events occur in the material. To reproduce these damage events in the CD model, the defect production rate has to be employed. Based on the work of Sand *et al*, the defect production term is expressed by a power law that relates the cluster size, n, and defect production rate, $G_{V,I}$ [23, 37], as shown in equation (2):

$$G_{V,I}(n) = \frac{A_{V,I}}{n^{S_{V,I}}}. \tag{2}$$

V is a vacancy, I is a self interstitial, $A_{V,I}$ is the pre-factor related to the total production rate, and G_{dpa}. $S_{V,I}$ denotes the scaling component [31, 38, 39]. The pre-factor, $A_{V,I}$, of the power law is calculated based on the total defect production rate, G_{dpa}, and is written as

Table 1. CD model mobility parameters for interstitial and vacancy defects.

Cluster	Pre-exponential factor ($m^2\ s^{-1}$)	Migration energy (eV)
I_1 (3D)	$D_0(I_1): 9.981 \times 10^{-11}$ [43]	0.165 [43]
I_2 (3D)	8.648×10^{-10} [43]	0.222 [43]
I_3 (3D)	3.47×10^{-10} [43]	0.203 [43]
I_4–I_∞ (1D)	$D_0(I_1)/n^{0.5}$, n is the number of SIAs in $^1/_2$<111> loop [44]	0.1 [43]
V_1(3D)	$D_0(V_1): 177 \times 10^{-8}$ [44]	1.66 [44]
V_2(3D)	$D_0(V_1)/2$ [45]	1.66 [44]
V_3(3D)	$D_0(V_1)/3$ [45]	1.66 [44]
V_4(3D)	$D_0(V_1)/4$ [45]	1.66 [44]
V_5–V_∞ (1D)	0	—

$$A_{V,I} = \frac{G_{\mathrm{dpa}}}{\sum_{n=1}^{N_{\max}} n^{1-S_{V,I}}}. \tag{3}$$

The parameters S_V and $S_I$are 1.63 and 2.20, respectively, obtained from the work of Sand *et al* [23, 37]. The maximum number of interstitials and vacancies ($N_{\max}$) is set to 60, determined based on the average values of the DB and AJ potentials, as described in the work of Wei *et al* [40].

The irradiation-induced defects in the CD simulation domain consist of self-interstitial atoms (SIAs), self-interstitial dislocation loop types of different Burgers vectors ($^1/_2$<111>, <100>), c15 clusters, vacancy and voids (vacancy clusters) [41, 42, 45]. SIA clusters comprising less than or equal to three SIAs and vacancy clusters containing vacancies below 5 ($\leqslant$4) have 3D motion. SIA clusters with size greater than 3 ($\geqslant$4) can be $^1/_2$<111> loops, <100> loops and c15 clusters. $^1/_2$<111> SIA loops can perform 1D migration while <100> loops and c15 clusters are considered as immobile defects. Voids containing more than 4 ($\geqslant$5) vacancies are treated as immobile defects. Vacancy-type dislocation loops have not been taken into account in the current study since the dislocation loops detected in the current experimental analysis are considered to be interstitial in nature. Moreover, in the experimental work of Klimenkov *et al* [17] with similar irradiation conditions, it was reported that dislocation loops are considered to be of interstitial type. The largest size of the c15 clusters considered in the CD model is 200 SIAs [41]. In the current CD, c15 clusters are nucleated through in-cascade clustering, and their subsequent evolution is governed by the absorption of migrating SIAs ($\leqslant$3) or the emission of SIA. Due to the thermal stability of c15 clusters, they collapse into loops when they are above certain critical sizes. The density dynamically varies due to the continuous nucleation and following collapse after growth over the critical size. Therefore, the partitioning of SIAs to c15 clusters was not high and relatively stable during irradiation. However, since the nucleation of c15 clusters constitutes a substantial proportion of all SIA clusters, their collapse plays a significant role in loop evolution. The CD model mobility parameters for interstitial and vacancy defects are reported in table 1.

The reaction for 3D configurational structures, such as c15 clusters and 3D migrating defects (I_1–I_3, V_1–V_4), are modeled using absorption coefficients, which are calculated using the following equation:

$$k_y^x = 4\pi\,(D_y + D_x)\,(r_y + r_x) \tag{4}$$

D is the diffusion coefficient and r is the reaction radius.

For the reaction between 3D migrating defects (x) and loops (y) involving reactants with non-spherical volumes, the reaction rate is evaluated based on equation (5) [46]:

$$k_y^x = (D_y + D_x)\left(\left(1-\alpha_y^x\right) z_{y,x}^L + \alpha_y^x\, z_{y,x}^V\right) \tag{5}$$

where

$$\alpha_y^x = \left(1+\left(\frac{r_y}{3(r_x+r_{\mathrm{d}})}\right)^2\right)^{-1},\ r_{\mathrm{d}} = \text{dislocation capture radius}$$

$$z_{y,x}^V = 4\pi\,(r_y + r_x + r_d)$$

$$z_{y,x}^L = \frac{4\pi^2 r_y}{\log\left(1+8r_y/(r_x+r_d)\right)}.$$

The interaction between 1D migrating defects is modeled using the reaction rate [46]

$$k_y^x = \frac{2D_y\sigma_{y,x}}{\lambda_y} \tag{6}$$

λ_y represents the mean free path of the 1D migrating defect calculated by $\lambda_y^{-1} = \sum_\omega \sigma_{y,\omega} C(\omega)$, where ω denotes the reaction of all defects and sinks with 1D migrating defects.

$\sigma_{y,x}$ denotes the cross-section of the reactants [46].

The emission coefficient (g_y^x) is calculated via the binding energy, E_b^x, and absorption coefficient, k_{y-x}^x, and it reads

$$g_y^x = \frac{1}{\Omega} k_{y-x}^x \exp\left(\frac{-E_b^x(y)}{k_B T}\right) \tag{7}$$

where k_{B} is Boltzmann's constant.

In order to obtain the binding energy of the single SIA and vacancy with the SIA and vacancy clusters, equations (8)–(11) are employed. $E_{\mathrm{f}}(n)$ is the formation energy of SIA clusters or voids, which consists of n SIAs or voids as shown in the following equations.

Binding energy of SIA cluster with SIA:

$$E_{\mathrm{b,SIA}}^{\mathrm{SIA}}(n) = E_{\mathrm{f}}^{\mathrm{SIA}}(1) + E_{\mathrm{f}}^{\mathrm{SIA}}(n-1) - E_{\mathrm{f}}^{\mathrm{SIA}}(n). \tag{8}$$

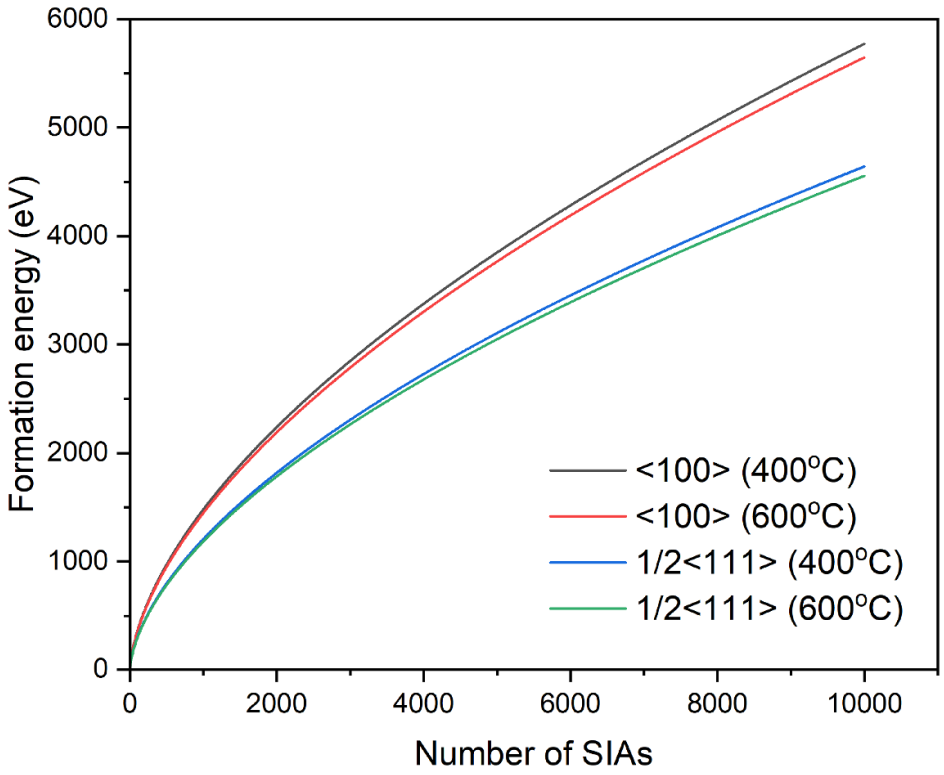

Figure 1. Formation energy of <100> and 1/2<111> loop at 400 °C and 600 °C calculated using dislocation elastic theory.

Binding energy of SIA cluster with vacancy:

$$E^{V}_{\mathrm{b,SIA}}(n) = E^{V}_{\mathrm{f}}(1) + E^{\mathrm{SIA}}_{\mathrm{f}}(n+1) - E^{\mathrm{SIA}}_{\mathrm{f}}(n). \quad (9)$$

Binding energy of vacancy cluster with SIA:

$$E^{\mathrm{SIA}}_{\mathrm{b},V}(n) = E^{\mathrm{SIA}}_{\mathrm{f}}(1) + E^{V}_{\mathrm{f}}(n+1) - E^{V}_{\mathrm{f}}(n). \quad (10)$$

Binding energy of vacancy cluster with vacancy:

$$E^{V}_{\mathrm{b},V}(n) = E^{V}_{\mathrm{f}}(1) + E^{V}_{\mathrm{f}}(n-1) - E^{V}_{\mathrm{f}}(n) \quad (11)$$

where $E^{V}_{\mathrm{f}} = 3.80$ eV [47], $E^{\mathrm{SIA}}_{\mathrm{f}} = 9.46$ eV [48].

In the case of voids, the formation energy is evaluated as

$$E^{V}_{\mathrm{f}}(n) = 4\pi (r_V)^2 \gamma \quad (12)$$

where $\frac{4}{3}\pi (r_V)^3 = n_v \frac{a_0^3}{2}$, a_0 is a lattice parameter, and γ is the surface energy.

The radii of the 1/2<111> and <100> loops [49] are calculated as follows:

Radius of <100> loop:

$$r_{100} = a_0 \sqrt{\frac{n_i}{2\pi}} + \Delta R_{\mathrm{c}}. \quad (13)$$

Radius of 1/2<111> loop:

$$r_{111} = a_0 \sqrt{\frac{n_i}{\sqrt{3}\pi}} + \Delta R_{\mathrm{c}}. \quad (14)$$

ΔR_{c} is the correction factor in the dislocation core position. It is calculated as $\frac{a_0}{2\sqrt{6}}$ and $\frac{a_0}{4}$ for 1/2<111> and <100>, respectively. n_i is the number of interstitials in the loop.

The radius of the void is calculated [27] as

$$r_v = \frac{D_{\mathrm{rec}}}{1+Z} + \epsilon + a_0 \left(\frac{3}{8\pi}\right)^{\frac{1}{3}} \left(n_v^{\frac{1}{3}} - 1\right) \quad (15)$$

where

The recombination distance, $D_{\mathrm{rec}} = a_0 \frac{\sqrt{3}}{2} + \epsilon$

ϵ =0.01 [27].

The bias factor, $Z = 1.2$ [27].

n_v is the number of vacancies in the void.

The loop formation energy, $E^{\mathrm{SIA}}_{\mathrm{f}}$, for the 1/2<111> and <100> loops is calculated based on the dislocation elastic theory for irradiation temperatures 400 °C and 600 °C as shown in figure 1 [50, 51]. The loop formation energies at 0 K were also calculated and compared with density functional theory (DFT) data for loop sizes smaller than 15 SIAs, showing good agreement between the dislocation elastic theory and DFT results [52]. In future work, the temperature-dependent surface energy will be considered to refine void formation energy calculations. The surface energy influences void stability and growth, and in the CD model, it affects the vacancy emission rate from a void by modifying the binding energy. Its temperature dependence is expected to impact the predicted void size distribution and overall defect evolution. By incorporating a more accurate temperature-dependent surface energy model, CD simulations will better capture the thermodynamic and

kinetic behavior of void formation under varying irradiation and thermal conditions.

Grain boundaries, dislocation lines and free surfaces are employed as sinks in the current model for 1D and 3D migrating defects [27]. The sink strengths for the defects implemented in the current study are described as follows:

Sink of dislocation lines [27]:

$$L_{dl,1D} = 2(\pi\,(r_d + r_{V,I})\,\rho_d)^2 \;\text{(1D migrating defect)} \tag{16}$$

$$L_{dl,3D} = \frac{2\pi\,\rho_d(1 - \rho^2)}{\ln(\frac{1}{\rho}) - 0.75 + 0.25\rho^2\left(4 - \rho^2\right)} \;\text{(3D migrating defect)} \tag{17}$$

where $\rho = (r_d + r_{V,I})\sqrt{\pi\,\rho_d}$.

Sink of grain boundary [27]:

$$L_{\mathrm{GB,1D}} = \frac{15}{R_{\mathrm{GB}}^2} \;\text{(1D migrating defect)} \tag{18}$$

$$L_{\mathrm{GB,3D}} = \frac{14.4}{R_{\mathrm{GB}}^2} \;\text{(3D migrating defect)}\,. \tag{19}$$

Sink of free surface [53]:

$$L_{\mathrm{surface,1D}} = \frac{8\cos^2\varphi}{l^2}\,\text{(1D migrating defect)}\,,\quad \varphi = 0 \text{ for the current work.} \tag{20}$$

$$L_{\mathrm{surface,3D}} = \frac{2}{l^2}\,\text{(3D migrating defect)} \tag{21}$$

where l is the thickness of the sample, φ is the angle of direction of loop migration and surface normal.

In experimental studies, it has been shown that irradiation-induced defects, like dislocation loops, are trapped by interstitial or substitutional atoms, which thereby impede its motion [17]. Within the trap sites, loops perform random walks in addition to the movement among lattice sites, and in order to take into account this phenomenon, an additional diffusivity term, D_i^{dt}, is incorporated based on equation (22) [36]:

$$D_i^{dt} = \upsilon_i^{dt}\frac{\lambda_i^2}{2N} \tag{22}$$

where λ is the hop length to account for the jump between trapping sites, which is assumed to be one-dimensional ($N = 1$), and υ_i^{dt} is the activation frequency. The hop length, λ_i, is inversely proportional to the trap density, ρ_t, r_i is the radius of the interstitial loop, and r_{t} is the length between the trap and mobile dislocation loop [36] as shown in equation (23):

$$\lambda_i = (4\pi\, r_i r_t \rho_t)^{-1}. \tag{23}$$

$^1/_2$<111> loops are treated as trapped and freely migrating loops in the present study. The free $^1/_2$<111> loops are modeled in CD in such a way that they can be trapped by the trapping elements in the course of motion. The CD model input parameters for W are reported in table 2.

Table 2. CD model input parameters for W.

Parameters	Value
Lattice parameter, a_0	0.316 nm [31]
Atomic volume	$a_0^3/2$ [29]
Burgers vector, b	0.274 nm [29]
Dislocation density, ρ_d	4–6 $\times$ 10^{12} m^{-2} [31]
Grain size, d	3 μm [31]
Dislocation capture radius, r_{d}	0.65 nm [45]
Dislocation bias, Z	1.2 [31]
Trap radius, r_{t}	1.5b [46]

In the study of Liu *et al* [42], during cascade, the majority of the dislocation loops formed in W are of interstitial type. In particular, different groups of interstitial clusters are categorized: (i) c15 clusters, (ii) $^1/_2$<111> loops, (iii) <100> loops, (iv) mixed structures comprising different Burgers vectors, (v) 'None' structures. At all PKA energies, most of the interstitial clusters observed are $^1/_2$<111> loop type, while at high energy cascades, a few <100> loop type and mixed structures are noted. Furthermore, the probability of c15 cluster formation increases with the increase of the PKA energy. In another study conducted by Liu *et al* [41], a detailed MD analysis was carried out to analyze the formation and stability of c15 clusters. In their study, it was shown that c15 clusters are immobile and highly stable once nucleated in W, and can collapse at high temperatures above 1500 °C to transform to $^1/_2$<111> loop type [41]. Moreover, in the event of collapse of c15 clusters, before the conversion of c15 cluster into $^1/_2$<111> loops at higher temperatures, the c15 clusters can transform into <100> loops at lower temperatures [41]. Based on the above study, the current work employed the formation of interstitial clusters, $^1/_2$<111> and <100> loops, SIA clusters of two and three SIAs and c15 clusters during irradiation cascades. The study assumed the formation of 5% c15 clusters, 1% <100> loops and the remaining as $^1/_2$<111> dislocation loops and SIA clusters comprising 2–3 SIAs. The dislocation loops ($^1/_2$<111>, <100>) and c15 clusters have more than four SIAs. However, mixed and 'None' structures are not taken into account in the irradiation cascade due to the insufficient data. In order to incorporate their role in the evolution of the defects, the percentage fraction of these interstitial structures is included in the dislocation loops ($^1/_2$<111>, <100>) and c15 clusters based on a similar approach to that employed in the study of Gao *et al* [45] (figure 4). The size distribution of defects produced due to irradiation cascades based on equations (2) and (3) is depicted in figure 2.

In the present study, the loop evolution in W by absorption and coalescence through interaction between loops of the same and different Burgers vectors is considered, as shown in figure 3. The following loop interactions are modeled in this study based on previous studies. The dislocation loops of interstitial type increase their size by absorbing SIAs or smaller mobile loops since the SIAs have a higher strain field than vacancies [14, 54]. Moreover, the growth of highly mobile $^1/_2$<111> loops occurs by absorbing or coalescing with smaller <100> loops. Similar mechanisms are considered for the

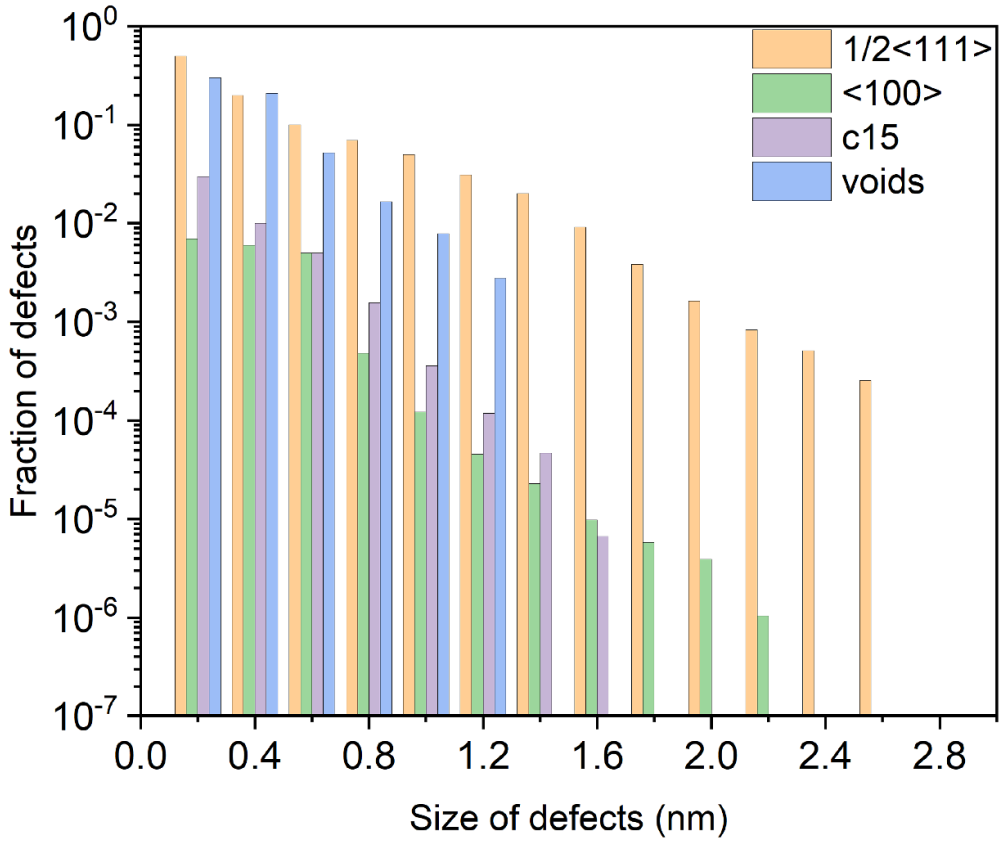

Figure 2. Size distribution of defects produced due to irradiation cascades.

<100> loops, in which a larger size of <100> loops can grow by absorbing smaller ½<111> loops. In fact, the populations of ½<111> and <100> loops are primarily governed by interactions between loops, with coalescence or growth resulting from the transfer of SIAs between them. The variants of ½<111> loops arise from the different possible orientations of the loops within the bcc crystal structure. The ½<111> direction has multiple equivalent orientations, leading to different ½<111> loop variants such as ½<111>, ½<$\bar{1}$11>, ½<1$\bar{1}$1> and ½<11$\bar{1}$>. Reactions between different ½<111> loop variants containing the same number of SIAs to obtain <100> loops are rare. However, the current study has incorporated this scenario and assigned a probability of ∼3/8 (3 c/(8 c-2)), where c is the concentration of each variant [45]. The remaining 5/8 between ½<111> loops of different variants and identical size yields ½<111> loops of larger sizes [45]. Reactions between loops with Burgers vectors ½<111> result in the formation of a loop with a Burgers vector of <100>, as shown in reaction (k) in figure 3. This reaction is expected to generate ½<111> loops, but instead, <100> loops are produced [55]. In this interaction, each ½<111> loop glides within the habit plane of the other interacting loop. Over time, both loops gradually merge into a single loop with a Burgers vector of <100 >.

The presence of interstitial impurity atoms and substitutional transmuted atoms in W plays an important role in the evolution of irradiation-induced voids and loops. In the case of pure W grade employed in the present study, despite having 99.7% purity, interstitial impurities such as C, H, He, N and O are observed with concentrations reported in the study of Bakaev *et al* [56]. Moreover, transmuted elements such as Re atoms are observed in the neutron-irradiated W sample employed for the irradiation reported in the previous and current studies [10, 16]. The impurities bind with vacancies and interstitial clusters and impede their movements. Therefore, the impurities act as traps for irradiation-induced mobile defects, which influence the overall microstructure of the material. It is thus important to incorporate interstitial impurity atoms and substitutional transmuted atoms in the current CD model. In the present study, trap elements with a concentration of 128 appm are employed as interstitial impurity atoms [56]. In addition, transmutation-based atoms with a density of 1.2×10^{14} cm^{-3} [16] are also modeled as trap elements. Moreover, the CD model considers only the interaction of ½<111> loops and mobile vacancies with the traps. The following differential equation (equation (24)) is used in the CD model to model the trapping of mobile ½<111> loops and mobile vacancies by the trapping elements,

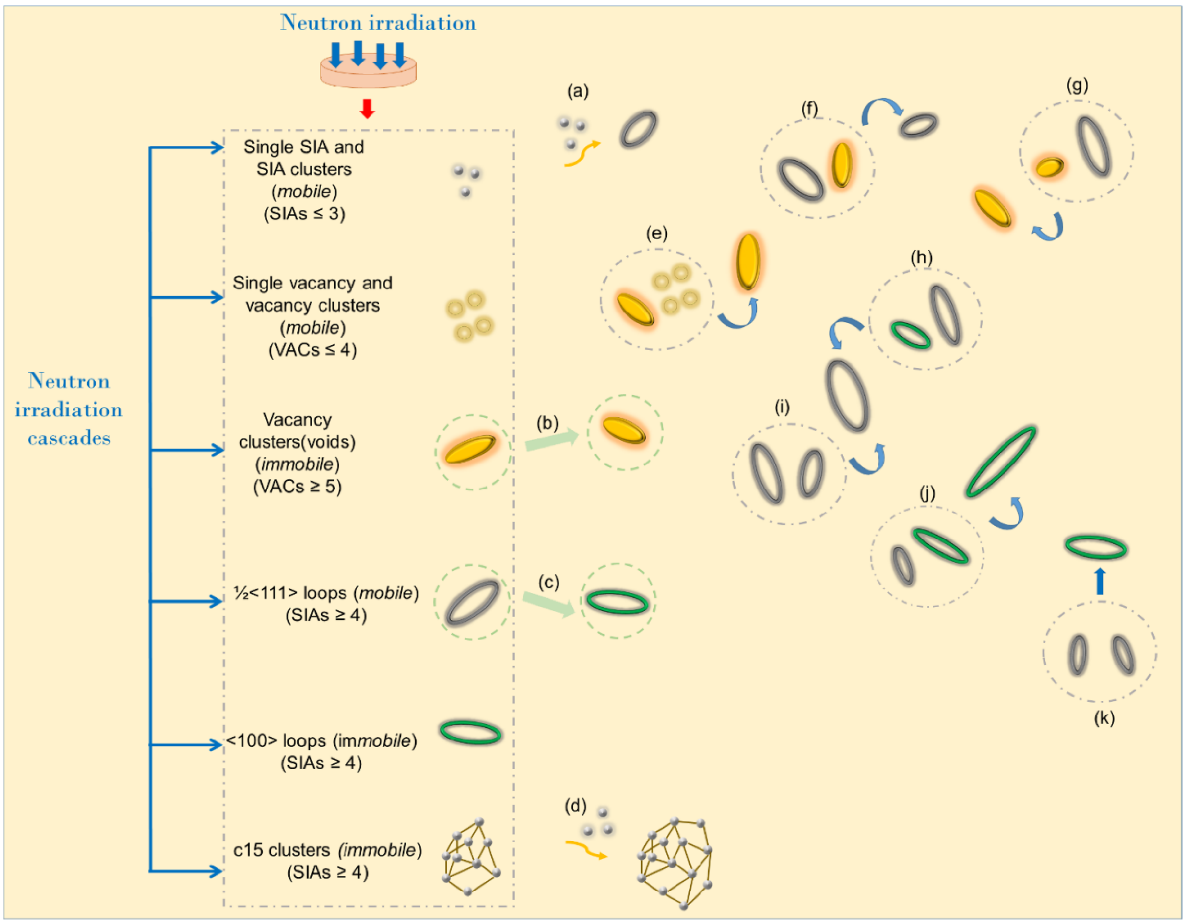

Figure 3. Illustration of defect kinetics involved in the evolution of irradiation-induced dislocation loops and voids. (*a*) Depicts the $^1/_2$<111> loop nucleation due to SIA migration, (*e*) depicts the nucleation of voids via migrating mobile vacancies, (*b*)–(*c*) illustrate the cascade overlap with pre-existing voids and dislocation loops that were formed during processes (*a*) and (*e*), (*d*) represents the nucleation of c15 clusters due to SIA migration, (*f*)–(*k*) depict the void or loop coalescence caused by 1D loop migration.

$$\frac{\mathrm{d}C_{\mathrm{trap}}}{\mathrm{d}t} = -k\_\mathrm{trap}\_L111\,(n_i)\,C_{\mathrm{trap}}C_{111}\,(n_i) - k\_\mathrm{trap}\_\mathrm{VAC}\,(n_v)\,C_{\mathrm{trap}}C_{\mathrm{VAC}}\,(n_v)\,. \quad (24)$$

C_{trap} is the density of trapping elements.

C_{111} is the concentration of the $^1/_2$<111> loop.

C_{VAC} is the concentration of the vacancy cluster ($\leqslant$4).

k_trap_VAC is the reaction rate between the trap and mobile vacancy cluster calculated based on equation (5). The radius of the trap is taken as 1.5b, where b is the Burgers vector.

k_trap_L111 is the reaction rate between the trap and $^1/_2$<111> loop calculated based on equation (6).

n_{i} is the number of interstitials.

n_{v} is the number of vacancies.

The first reaction term represents the reduction in trap density due to the trapping of $^1/_2$<111> loops. In this model, each trap is assumed to accommodate only a single loop, leading to its permanent removal from the available trap population upon capturing a defect.

During neutron irradiation, transmutation reactions generate helium atoms, which exhibit low solubility and high mobility within metal lattices [57]. Helium primarily affects the mechanical properties of metals by promoting the formation of helium-stabilized cavities along grain boundaries at elevated temperatures [58]. A key role of helium is facilitating cavity nucleation and growth, ultimately leading to void swelling. Experimental studies and *ab initio* calculations in α-Fe reveal a strong interaction between vacancies and helium atoms, as well as helium–vacancy (He–V) clusters, highlighting the significant contribution of helium to the stabilization of vacancy clusters [58]. As helium accumulates within these voids, the internal gas pressure increases, further driving void growth and material swelling [59]. Additionally, helium influences void coalescence, impacting the overall void distribution and structural stability [60]. In this study, helium production via the (n,α) reaction is not explicitly considered in the simulation, as the predicted helium generation rate under the given irradiation conditions is low, estimated at 1–2 appm He/dpa.

2.2. Numerical algorithm

The model employs the Jacobian matrix of the ordinary differential equation (ODE) system using the analytical form, $J_{ij} = \partial\left(\frac{\partial C_i}{\partial t}\right)/\partial C_j$, where C_i and C_j are the densities of clusters. The solution of the Jacobian matrix is evaluated by means of python wrappers of the odespy package [61] based on

the odepack algorithms [62]. In order to model large defect clusters, a higher number of differential equations has to be coupled to calculate the solution. To speed up the computational process and time, a grouping method is employed, which implements two equations per cluster group to achieve conservation of mass and the cluster density [63]. The present study employs loop and void sizes of a maximum of 3000 SIAs and vacancies in the CD model.

3. Results

3.1. Experiment

For the experimental analysis, an ITER-grade stress-relieved IGP-W bar, dimensions 36 × 36 × 480 mm^3 with 99.7 wt% purity produced by PLANSEE SE, Austria, is implemented [10]. Disk-shaped compact tension (DCT) W specimens with 4 mm thickness are fabricated using an electrical discharge machining transverse to the forging direction [10]. Irradiation experiments are performed on DCT specimens placed in the fuel channel of the Material Test High Flux BR2 reactor of SCK-CEN in Mol, Belgium. Experiments are performed for irradiation doses of ∼1 dpa with the neutron fluence as depicted in table 3 at irradiation temperatures of 400 °C and 600 °C followed by TEM characterization of irradiation-induced defect features. The calculation of the irradiation dose in displacement per atom (dpa) units was performed by MCNPX 2.7.0 [64] for a threshold displacement energy of 55 eV in W. The ALEPH code of SCK-CEN [65] and accessible nuclear databases are applied for the calculation of transmuted elements such as rhenium (Re) and osmium (Os) [66–68]. More details on these calculations can be found in the study of Yin *et al* [69]. For microstructural investigations, a FEI Scios focused-ion beam (FIB) scanning electron microscop was utilized to prepare TEM lamellae from the undeformed region of the DCT specimens. Several TEM lamellae were lifted out *in situ* and attached onto the molybdenum TEM half-grid by Pt deposition. Finally, the lamellae were thinned down to electron transparency (to a thickness of 50–150 nm) with multiple passes of a low-energy ion beam. The FIB-induced damage was minimized by optimizing the cleaning pattern procedure parameters. A high-resolution FEI Tecnai G2 F20 X-TWIN microscope operating at 200 kV equipped with a Gatan double-tilt holder and a high-angle annular dark-field (HAADF) scanning TEM (STEM) detector was employed for quantitative characterization of dislocation loops and voids. For the statistical analysis of the dislocation loops via the application of g •b criteria, weak-beam dark field (WBDF) images were acquired for different diffraction vectors g. An excitation error s_g of approximately 0.2 nm^{-1} was employed. The identification of a void and its statistics were obtained by the traditional through-focal series technique, where the contrast of the void changes from a white dot with a black fringe in an under-focused image to a dark dot with a white Fresnel fringe in an over-focused image. The thickness of the areas of interest was determined by electron energy loss spectroscopy with an uncertainty of ∼10%. The estimated error involved in the measurement of defects using TEM was found to be ±30% loop density via WBDF, ±0.6 nm loop size via WBDF, ±5% void density and ±0.2 nm void size. In addition, a Thermo Fisher Scientific Talos F200X microscope equipped with an energy dispersive spectroscopy (EDX) detector was employed for analytical TEM to examine the spatial distribution of the transmutation products.

3.2. TEM characterization of irradiation defects

Figures 4(*a*) and (*b*) show an overview of the dislocation loop microstructure in the IGP-W after irradiation to 1 dpa at 400 °C. For the quantitative analysis of loops, several images were acquired and analyzed under WBDF conditions. For instance, a representative WBDF micrograph (figures 4(*a*) and (*b*)) taken under $g = \{110\}$ and $\{002\}$ diffraction conditions presents clear dislocation loop features with a mainly elliptical shape where the major axis of the loop is taken as a measure of its size. Here, $g = \{110\}$ and $\{002\}$ diffraction vectors were analyzed, resulting in a total loop density of 2.57×10^{16} cm^{-3} and a mean size of 3.50 nm. By applying the loop invisibility criteria and the statistical method for Burgers vector determination, the visible loops were found to be of both $1/2<111>$ and $<100>$ types, with 53% and 47% fractions, respectively. Owing to the resolution limit under WBDF conditions, loop sizes less than 2 nm are excluded in the statistical analysis. The size distribution of the dislocation loops under WBDF conditions with $g = \{110\}$ diffraction vector is presented in figure 7(*b*). Figures 4(*c*) and (*d*) present the overall microstructure of the as-irradiated (1.06 dpa, 600 °C) IGP-W acquired via the WBDF technique under $g = \{110\}$ and $\{002\}$ diffraction conditions, manifesting a high density of nm-sized black dots and interstitial dislocation loops. Typical loop features with a circular/elliptical shape and coffee bean contrast are identified. Black dots are not counted in the WBDF micrograph. For the statistical analysis of loops, the total dislocation loop density and mean size are found to be $\sim 3.10 \times 10^{16}$ cm^{-3} and 3.07 nm, respectively. Furthermore, as most defects (≤2 nm) show black dot features, which are difficult to resolve in TEM even via the WBDF technique, only defects with characteristic features (figures 4(*c*) and (*d*)) were counted as dislocation loops. Moreover, the $<100>$ loop fraction is found to be about 31%, which is calculated via the statistical method for Burgers vector determination based on the invisibility criteria ($g \cdot b = 0$). The size distribution of dislocation loops determined for the $g = \{110\}$ diffraction vector is presented in figure 7(*c*).

Similar to the high density of dislocation loops, the majority of nano-sized voids were found to be uniformly distributed in the as-irradiated sample, as presented in the under-focused bright field (BF)-TEM micrograph in figure 4(*e*) for 400 °C. The mean void diameter (fringe edge-to-edge distance) is estimated to be 1 nm, and the density is determined to be 1.9×10^{17} cm^{-3}. Figure 9 shows the void size distribution in which most voids are less than 2 nm. In addition, it is noteworthy that many voids with sizes less than 1 nm are hardly determined via the through-focal series technique with defocus conditions of about ± 1 nm. WBDF imaging exhibits high sensitivity to small defects by enhancing the contrast of lattice distortions,

Table 3. Irradiation conditions in experimental analysis.

T_{irr} (°C)	Irradiation time (days)	Flux (n cm^{-2} s^{-1}) ($E > 0.1$ MeV)	Flux (n cm^{-2} s^{-1}) ($E > 1$ MeV)	Flux (n cm^{-2} s^{-1}) (0.1 $< E <$1 MeV)
400	186	1.9×10^{14}	8.9×10^{13}	1.0×10^{14}
600	186	2.3×10^{14}	1.1×10^{14}	1.2×10^{14}

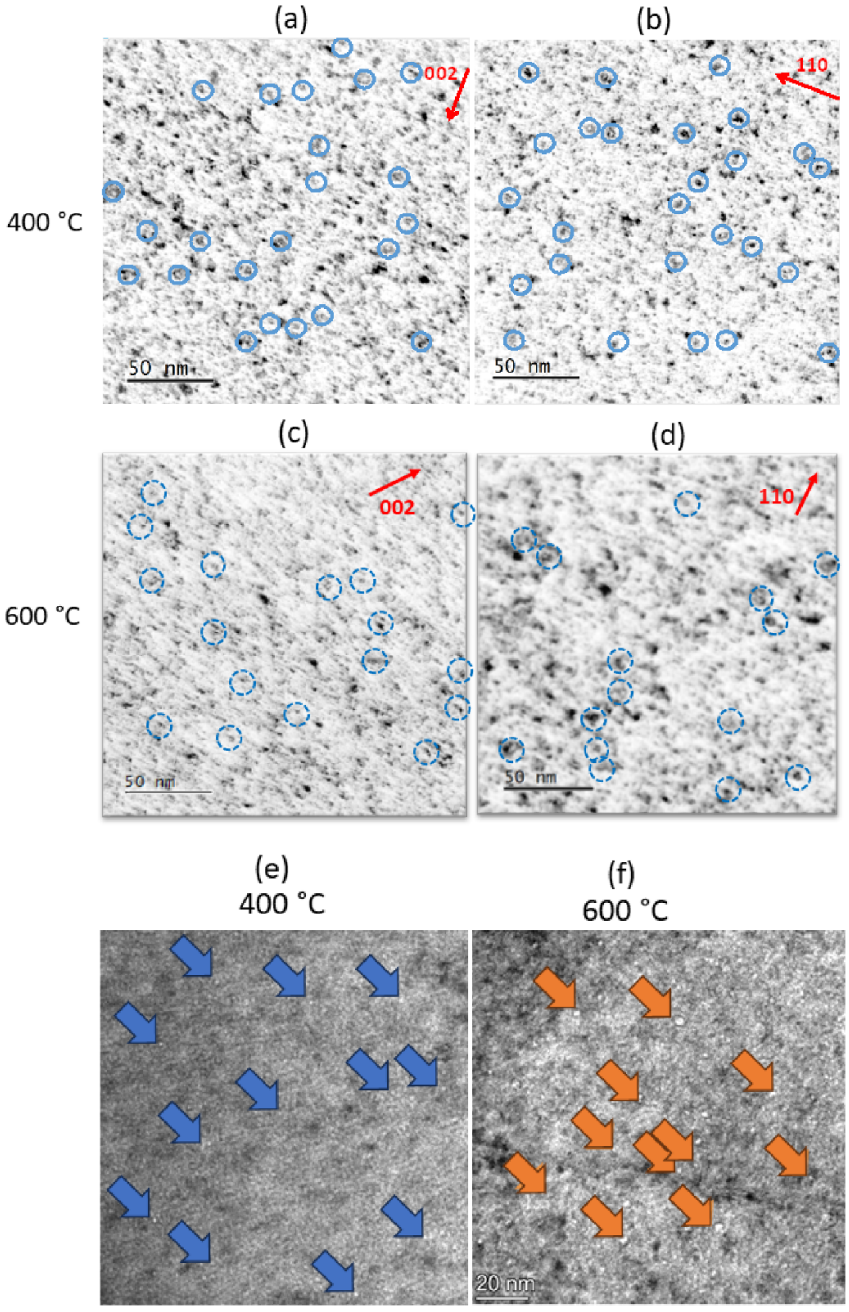

Figure 4. Dislocation loop and void microstructures in irradiated IGP-W. WBDF micrograph taken under (*a*) $g = \{002\}$ diffraction condition at 1.02 dpa, 400 °C, (*b*) $g = \{110\}$ diffraction condition at 1.02 dpa, 400 °C, (*c*) $g = \{002\}$ diffraction condition at 1.06 dpa, 600 °C, (*d*) $g = \{110\}$ diffraction condition at 1.06 dpa, 600 °C manifesting a high density of black dots and dislocation loops with near-circular, elliptical and coffee bean contrast (encircled); typical BF-micrographs presenting void distribution in irradiated IGP-W at (*e*) 1.02 dpa, 400 °C, (*f*) 1.06 dpa, 600 °C.

allowing the detection of voids as small as 0.25 nm. Although the focal series technique has limitations in resolving voids below 1 nm, the WBDF imaging conditions used in this study enabled the measurement of some sub-nanometer voids. However, the detection of smaller voids (<1 nm) using WBDF imaging directly may involve non-trivial errors compared to

Table 4. Dislocation loop and void statistics obtained from the experiment.

Type of defect	T_{irr} (°C)	Mean size (nm)	Total density (cm^{-3})	$^1/_2$<111> (%)	<100> (%)
Dislocation loop (interstitial type)	400	3.50	2.57×10^{16}	53	47
	600	3.07	3.10×10^{16}	69	31
Void	400	1.00	1.90×10^{17}	—	—
	600	0.90	2.10×10^{17}	—	—

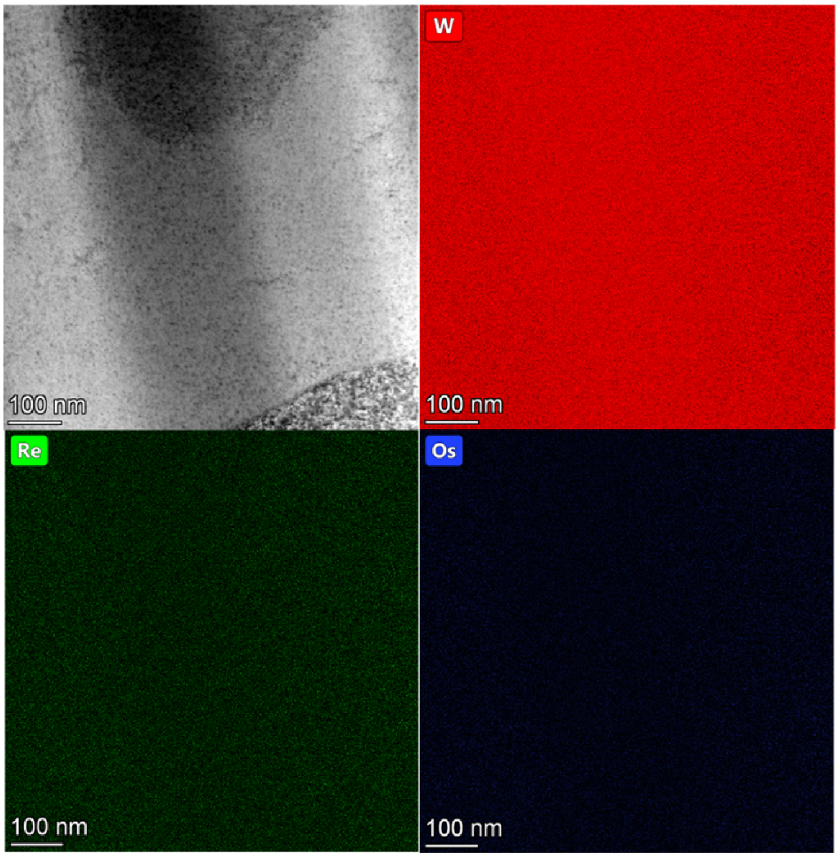

Figure 5. Representative STEM-HAADF micrographs with inverted contrast, for irradiated (1.02 dpa, 400 °C) IGP-W along with corresponding STEM-EDX spectrum images providing elemental mapping, with W highlighted in red and transmutation-induced Re in green, along with Os in blue.

the focal series technique. For 600 °C, in addition to a few dislocation loops/black dots, several marked voids are identified near the grain boundary (figure 4(*f*)). This indicates that there is no clear void denuded zone near the grain boundaries in the as-irradiated condition. The mean void diameter (fringe edge-to-edge distance) is estimated to be 0.9 nm and the density is determined to be $\sim 2.1 \times 10^{17}$ cm^{-3}. The size distribution of voids is presented in figure 9. The statistics regarding the dislocation loops and voids are reported in table 4.

As the content of transmutation products Re (Os) in the as-irradiated condition is expected to be at the level of 2 at% (0.2 at%) [66–68], STEM-EDX analysis was conducted to visualize their distribution. No evidence of Re or Os decoration or segregation at grain boundaries was observed at 400 °C, as depicted in figure 5. Additionally, there was no evidence of precipitation within the grains. Notably, the investigated as-irradiated sample exhibited approximately 2.4 at% Re as confirmed by elemental mapping.

Elemental mapping (figure 6) shows neither Re/Os decoration/segregation nor precipitation at grain boundaries and/or in the grains of the sample after irradiation at 600 °C. In addition, elemental quantification analysis shows that about 1.9 at% Re is detected in the selected grain (see marked frame in figure 6), which indicates that Re, Os and their TEM-invisible clusters are uniformly distributed in the sample.

3.3. Cascade parameters implemented for CD model

Irradiation damage in nuclear materials caused by collision cascades is reported in several studies [70, 71]. During continuous irradiation of the material, the collision cascades overlap with the pre-existing defects and can actually change the

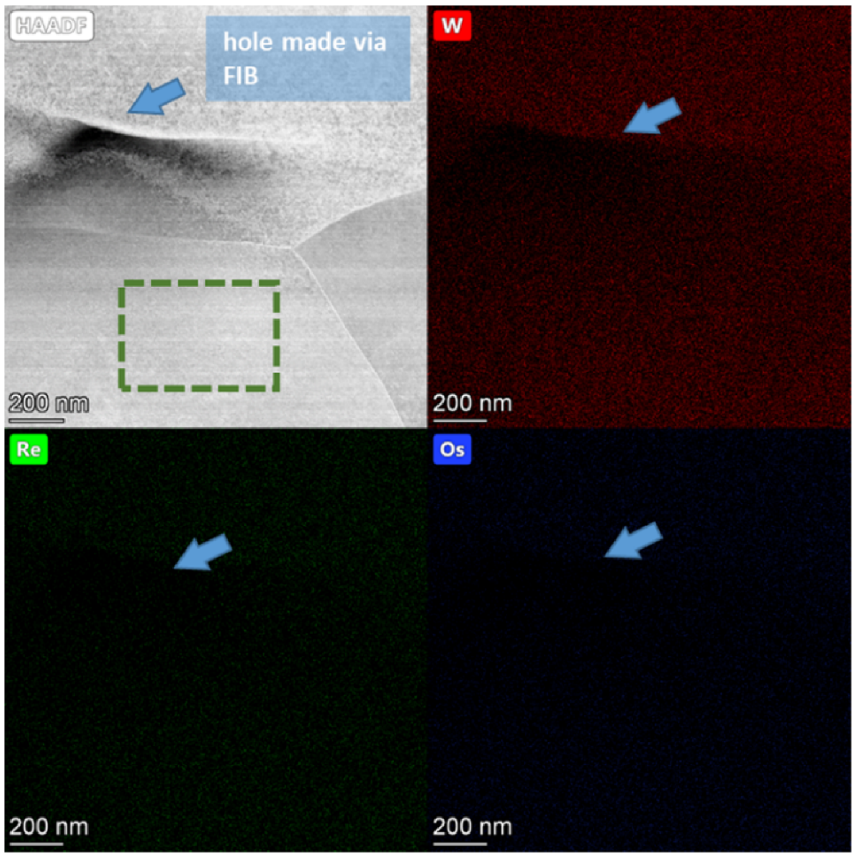

Figure 6. Representative STEM-HAADF micrograph of irradiated IGP-W (1.06 dpa, 600 °C) showing grain boundaries. STEM-EDX spectrum images show the corresponding elemental mapping of W (red) and transmutation induced Re (green) and Os (blue).

morphology and the size of the defect clusters in the irradiated material [70]. In fact, there is a reduction in the defects formed during cascade overlap in an irradiated material with respect to the number of defects produced in a pristine material during the initial cascades, which is corroborated in various studies [70, 71]. Moreover, the cascade overlaps can be categorized into partial overlaps and full overlaps [70]. In the case of partial cascade overlap, there is a drastic decrease in the defect cluster size, while for full cascade overlap the average decrease in the defect cluster size is lower. The present study incorporates the influence of full cascade overlap on the pre-existing defect distribution in the W material. In order to realize a cascade overlap event, the transformation of the SIA cluster ($^1/_2$<111> and <100>) type is implemented in the CD model by means of transformation coefficients as implemented in the following governing equation for $^1/_2$<111> and <100> loops (equation (25)). The transformation coefficients represent the probability of transformation of the $^1/_2$<111> and <100> loop into <100> or $^1/_2$<111> loop types. The information regarding the transformation coefficients is taken from the study of Byggmastar *et al* [70]. In the event of cascade overlap, there are also changes in the defect cluster morphology, with the formation of mainly $^1/_2$<111>, <100>, mixed and 'None' clusters. In fact, mixed clusters include dislocation loops of different Burgers vectors ($^1/_2$<111>, <100>). The presence of mixed clusters is observed in the collision cascade simulations [70]. However, these mixed clusters are unstable and can transform into other loop types after annealing. In the case of 'None' structures, there is no information regarding their stability during a cascade overlap event in W. Due to scarce data on the mixed and 'None' clusters regarding their morphology and size, the current study has not considered their in the cascade overlap event. Moreover, the cascade overlap event on the c15 clusters and its transformation are not considered since there is insufficient information on the transformation coefficients.

It is important to emphasize that defect production decreases when a cascade overlaps with SIA clusters [70]. Additionally, the size of the SIA cluster is reduced compared to its original size after an overlap event. These effects are not included in the CD model because the number of overlapping events is expected to be minimal in relation to all cascade events. Furthermore, SIAs lost from the original clusters during the cascade overlap are expected to diffuse and be absorbed by nearby SIA clusters [45]. In the current work, the influence of full cascade overlap is taken into account to understand the microstructural evolution of loops and voids in W. In order to incorporate the full cascade overlap event, the cascade overlap rate (F_{ol}) is included in the CD model, which considers the probability of a full cascade overlap event per unit time

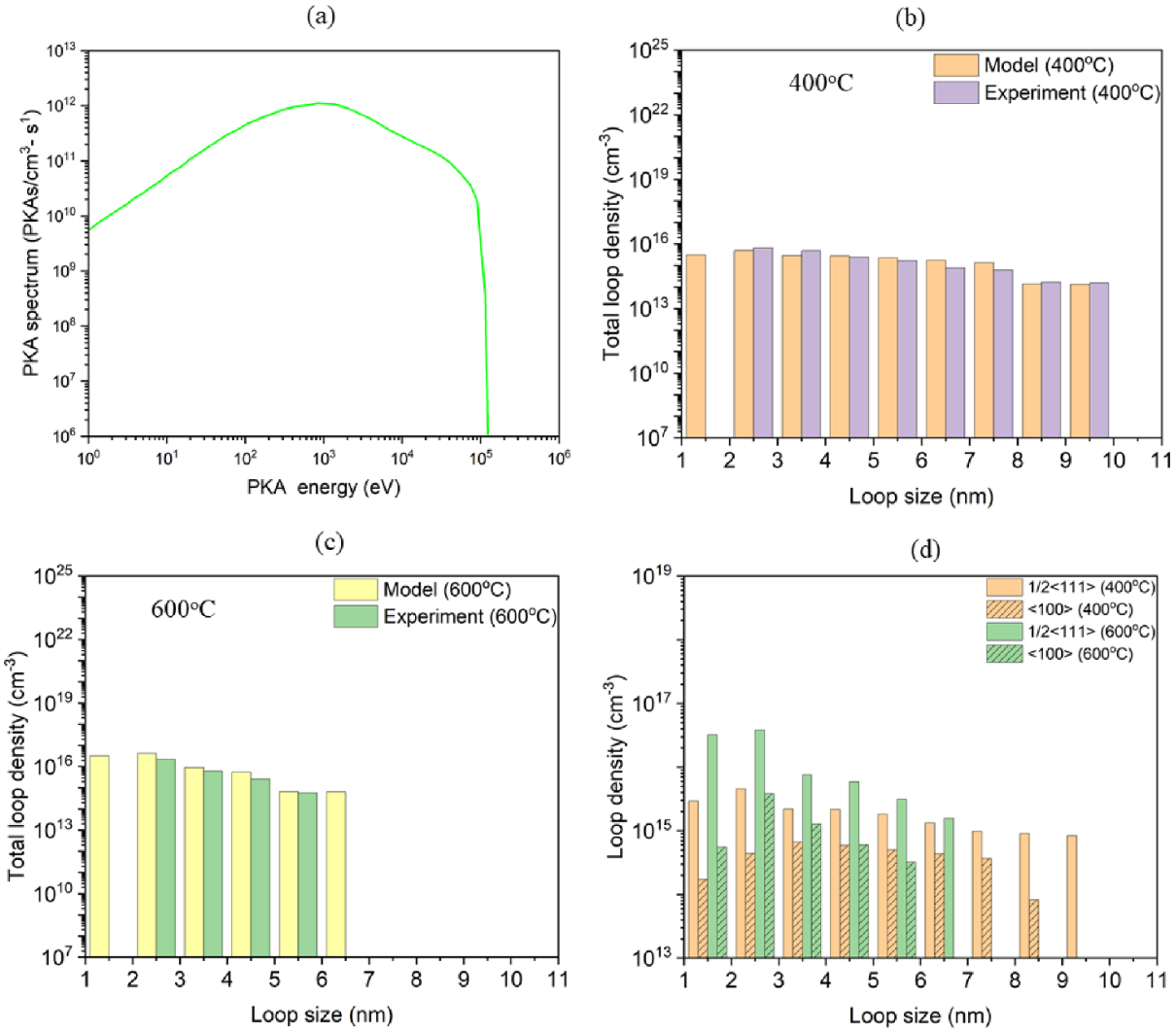

Figure 7. (*a*) PKA spectrum from SPECTRA-PKA across the DCT specimen based on the experimental irradiation conditions. Total loop density vs loop size obtained from experimental and CD model at (*b*) 400 °C (loop sizes from the CD model that fall below the observable limits of experimental testing are considered as black dots.) (*c*) 600 °C (loop sizes from CD model below the observable limits of experimental testing are considered as black dots) for 1.02 dpa. (*d*) 1/2<111> and <100> loop density from CD model at 400 °C and 600 °C for 1.02 dpa.

based on equation (25) [45]:

$$\frac{\mathrm{d}C_{100}(n)}{\mathrm{d}t} = \epsilon + f_{111\,\mathrm{to}\,100}(n)\,F_{ol}(n)\,C_{100}(n) - f_{100\,\mathrm{to}\,111}(n)\,F_{ol}(n)\,C_{111}(n) \qquad (25)$$

where ϵ represents the terms on the right-hand side of equation (1), and $f_{111\,\mathrm{to}\,100}(n)$ and $f_{100\,\mathrm{to}\,111}(n)$ represent the transformation of a 1/2<111> loop to a <100> loop and a <100> loop to a 1/2<111> loop, respectively, during cascade overlap. Similarly, differential equations are also employed for <100> loops and voids.

In the present study, the cascade overlap rate is calculated based on approximation in terms of the experimental flux and volume of the cascade-induced molten domains in the damaged region. In a previous study conducted by De Backer *et al* [72] using numerical models, cascade simulations were carried out to formulate a relationship which shows that there is a linear relationship between the total volume of the molten domain (V_{mol}) and the PKA (E_{PKA}) energy, $V_{\mathrm{mol}} = a^{*}E_{\mathrm{PKA}}$ and $a = V_{\mathrm{fr}}/E_{\mathrm{fr}}$, where V_{fr} is volume of the molten domain at the cascade fragmentation energy (E_{fr}), which is 160 keV [72]. V_{fr} is 10^{6} A^{o3} at the threshold E_{fr}.

In order to obtain F_{ol}, the neutron flux spectrum from the experiment (reported in table 3) is employed in SPECTRA-PKA [73] code to analyze the PKA spectrum for a range of PKA energy. The PKA spectrum is generated employing TENDL-2017 [74] pre-processed nuclear data, which consist of recoil matrices for W shown in figure 7(a). Based on the linear relationship, $V_{\mathrm{mol}} = a^{*}E_{\mathrm{PKA}}$, and V_{mol} is calculated using E_{PKA} and multiplied by the PKA spectrum for values above

E_{fr} to obtain the average cascade overlap rate, F_{ol}, which is around $5 \times 10^{-7}\,s^{-1}$.

3.4. Comparison of CD model results with experimental data

Figures 7(*b*)–(*d*) and figure 9 depict the total loop and void density distribution and their comparison between the experiment and numerical results at irradiation temperatures of 400 °C and 600 °C. The results obtained from the numerical model are able to reproduce the trend of dislocation loops ($^1/_2$<111>+<100>) and voids from the experimental data in terms of the loop and void sizes (figures 7(*b*)–(*d*) and 9). The CD simulation is able to predict the loop sizes up to 10.5 nm as observed in the experimental observations for 400 °C. However, for 600 °C, higher loop sizes are noted in the CD results, which are not observed in experiments. This could be due to the use of only a limited number of temperature-dependent parameters. In future work, attempts will be made to calculate more temperature-dependent parameters (similar to the calculation of formation free energy) to improve the CD model. Moreover, loop sizes less than 2 nm are not measured in the experiment, while in the numerical results, loop sizes less than 2 nm are included. The treatment of trapped elements such as interstitial impurities and substitutional transmuted elements in the CD model also influence the results. Since the concentration of impurities is less due to the 99.7% pure W sample, the role of irradiation-induced transmuted elements can influence the numerical results. In order to study the actual migration of the transmuted elements and their interaction with the loops and voids, separate ODEs are required for transmuted elements, which need to be coupled in the CD model, which can be computationally expensive. Since the main objective of the current study is to analyze the long-term evolution of the loops and voids in W material, transmuted elements are only considered as traps. Moreover, due to the lack of data on the mixed and 'None' clusters and based on some assumptions, these clusters are integrated in $^1/_2$<111>, <100> loops and c15 clusters as percentage fractions.

A comparison between the experimental and numerical results of loop density is shown in figures 7 (*b*) and (*c*). In the case of the numerical results, loop sizes of less than 10 nm and 7 nm are obtained in the model at irradiation temperatures of 400 °C and 600 °C, respectively. A <100> loop size up to 8.5 nm and a $^1/_2$<111> loop size of less than 10 nm are predicted in the model, as depicted in figure (7(*d*). However, based on the experimental observations, the difference between the total loop density at 400 °C and 600 °C is not very significant (2.57×10^{16} cm^{-3} (400 °C) and 3.10×10^{16} cm^{-3} (600 °C)). It should be noted that the main difference for the irradiation temperatures of 400 °C and 600 °C is the $^1/_2$<111> and <100> loop population. As mentioned in the loop statistics from the experiment reported in table 4, at 600 °C, the $^1/_2$<111> loop population (69%) is higher than the <100> loop population (31%). At 400 °C, the difference between the $^1/_2$<111> and <100> loop population is relatively smaller (47% <100> and 53% $^1/_2$<111>). In terms of the ratio between the $^1/_2$<111> and <100> loop density, ratios of 1.1 and 2.3 are obtained for 400 °C and 600 °C, respectively. Based on the experimental observations, a similar trend in the $^1/_2$<111> and <100> loop populations is observed in the numerical results. In particular, from the CD model results, the ratio between the $^1/_2$<111> and <100> loop density is around 5.43 and 13.5 at 400 °C and 600 °C, respectively (figure 7(*d*)). Additionally, both the experimental and numerical results show that the $^1/_2$<111> loop density at 600 °C is higher than at 400 °C. The formation energy of $^1/_2$<111> loops is lower than that of <100> loops. As the temperature rises, the formation energy of $^1/_2$<111> loops decreases further, implying that less energy is needed for their formation. This makes them more likely to form at elevated temperatures compared to <100> loops.

At the early stages of irradiation, higher SIA diffusivity facilitates nucleation by allowing mobile SIAs to aggregate more efficiently into small clusters before being absorbed by sinks [75]. This leads to a higher initial density of $^1/_2$<111> loops, where enhanced defect mobility promotes the formation of new loops. However, at later stages of irradiation, when the nucleation phase is complete, higher diffusivity is expected to favor growth rather than further nucleation. Therefore, more mobile SIAs should contribute to the continued enlargement of existing loops instead of forming new ones. Despite this, the growth of $^1/_2$<111> loops may not be significantly enhanced due to SIA–vacancy recombination, absorption by <100> loops and sinks such as grain boundaries, dislocation networks and surfaces [76].

At higher temperatures like 600 °C, vacancies become more mobile, leading to faster recombination with SIAs, reducing the effective flux of SIAs available for loop growth. Additionally, larger <100> loops serve as stronger sinks, capturing mobile SIAs, which limits the growth of $^1/_2$<111> loops. Over time, other microstructural sinks such as dislocations, grain boundaries and surfaces absorb SIAs, diverting them away from loops and reducing their chances to grow.

Figures 8(*a*)–(*c*) illustrate the evolution of $^1/_2$<111> and <100> loops in terms of density, average size and the number of SIAs (N_{SIAs}) accommodated by the loops as a function of the irradiation dose. Figure 8(*d*) depicts the fraction of interstitials associated with loops, sinks (grain boundaries, dislocation network and surface) and c15 clusters. The CD model predicts that the average size of $^1/_2$<111> and <100> loops ranges between 1.5 and 3.5 nm (figure 8(*b*)).

At 400 °C, there is an increase in the $^1/_2$<111> loop density up to 0.2 dpa with a consequent decrease in N_{SIAs} (figures 8(*a*) and (*c*)). The peak that arises in the N_{SIAs} is due to the reduction in $^1/_2$<111> loop density at 400 °C beyond 0.2 dpa (figures 8(*a*) and (*c*)), which occurs as smaller $^1/_2$<111> loops are progressively absorbed by enlarged immobile <100> loops. This absorption leads to a decline in N_{SIAs} within $^1/_2$<111> loops (figure 8(*c*)), while simultaneously promoting an increase in the size of <100> loops (figure 8(*b*)). As irradiation continues, the nucleation of newly formed <100> loops results in a net increase in their density (figure 8(*a*)), which is further accompanied by an increase in N_{SIAs}, as seen in figure 8(*c*). At 400 °C, the availability of smaller $^1/_2$<111> loops diminishes due to their high mobility, leading to their absorption by <100> loops and sinks (grain

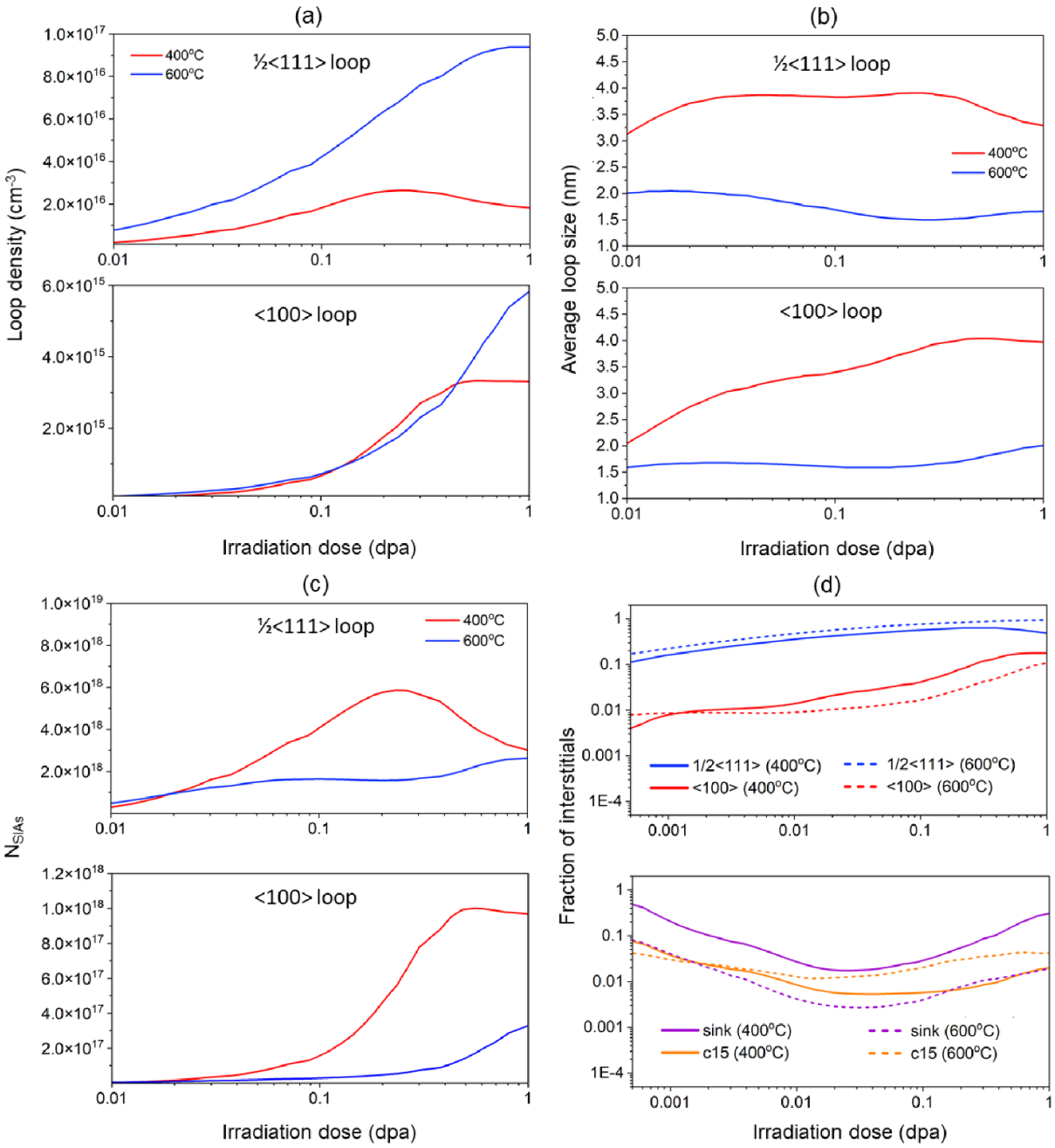

Figure 8. CD model results as a function of irradiation dose (dpa) for (*a*) $^1/_2$<111 > and <100> density, (*b*) average loop size, (*c*) SIAs in $^1/_2$<111> and <100> (in cm^{-3}), (*d*) fraction of interstitials accommodated by sink (grain boundaries, dislocation network and surface), c15 clusters, $^1/_2$<111> and <100> loops.

boundary, dislocation network, surface) (figure 8(*d*)). This reduction in available SIAs slows down the further growth of the size and density of <100> loops, leading to a near steady-state behavior at a dpa above ∼0.5, as shown in figure 8(*c*).

At 600 °C, the increased mobility of SIAs facilitates their clustering, resulting in a higher nucleation of $^1/_2$<111> loops. Consequently, this leads to a higher density of $^1/_2$<111> loops (figure 8(*a*)). However, despite the increased density at 600 °C, the growth of existing $^1/_2$<111> loops is not significantly enhanced. The greater mobility of vacancies at this temperature accelerates SIA–vacancy recombination, reducing the number of mobile SIAs available for further loop growth. Although $^1/_2$<111> loops may form further, their continued expansion is suppressed as SIAs are absorbed by larger <100> loops and sinks (grain boundary, dislocation network, surface), limiting their overall growth. Regarding the evolution of c15 clusters, the fraction of SIAs accommodated by $^1/_2$<111> loops is higher than that by c15 clusters (figure 8(*d*)). Up to approximately 0.5 dpa, the fraction of SIAs in c15 clusters decreases at both 400 °C and 600 °C as more migrating SIAs are absorbed by loops ($^1/_2$<111> and <100>), reducing the number available for c15 clusters. After

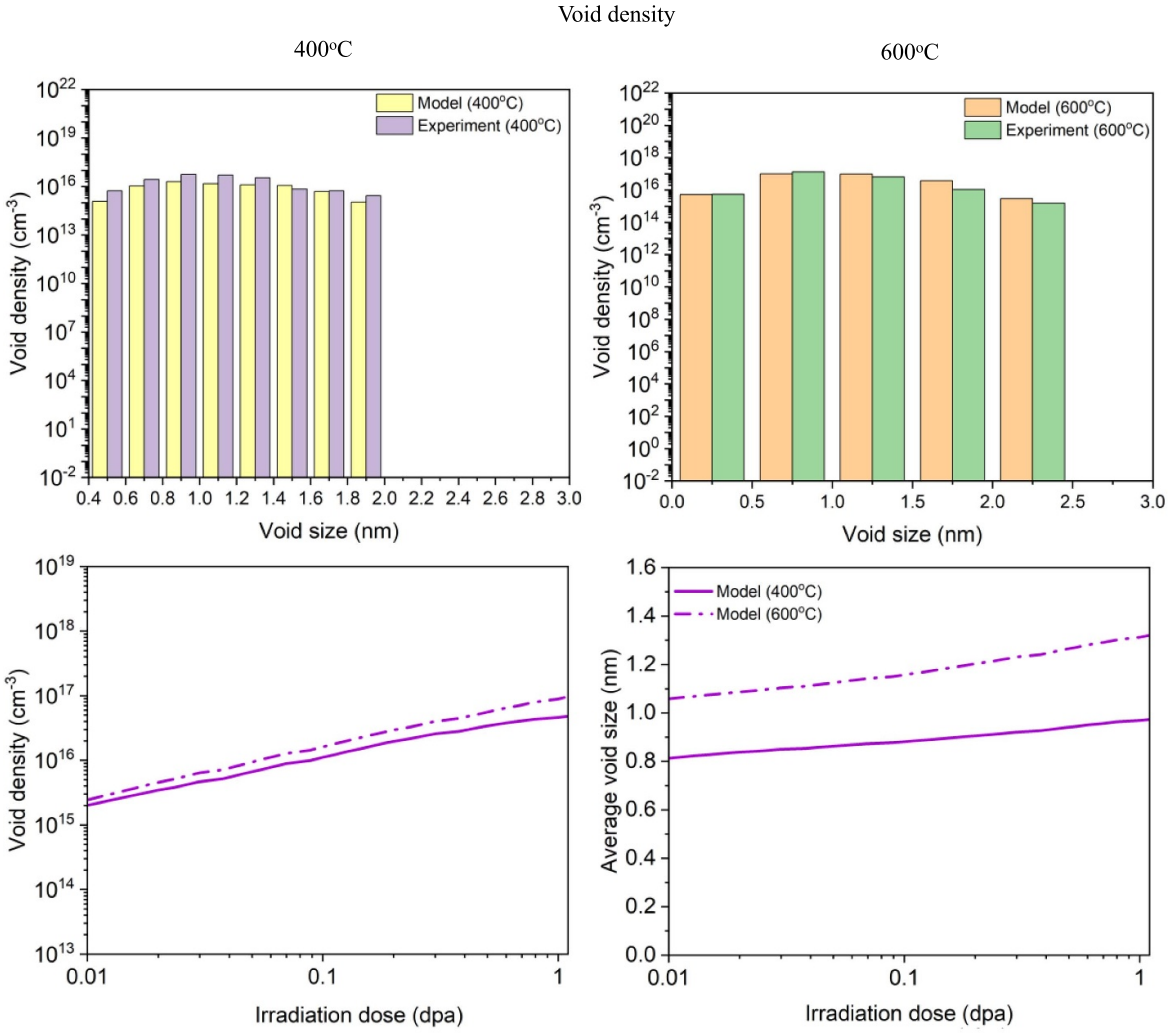

Figure 9. Void density vs void size obtained from experimental and CD model at 400 °C and 600 °C for 1.02 dpa (top), CD model results as a function of irradiation dose (dpa) for void density (left, bottom) and average void size (right, bottom).

0.5 dpa, the fraction of SIAs in c15 clusters increases due to the higher absorption of mobile SIAs (figure 8(*d*)).

In the case of voids, the model predicts well the density distribution at 400 °C and 600 °C with respect to experimental observations (figure 9). The density and average size of voids from the CD results as a function of the irradiation dose at 400 °C and 600 °C are depicted in figure 9 (bottom). It should be noted that at 600 °C, the void size increases compared to at 400 °C. This is primarily because, at higher temperatures, mobile vacancies ($\leqslant$4) exhibit increased diffusivity, allowing them to coalesce with immobile voids and thereby increase their size.

3.5. Influence of the cascade overlap

To analyze the overlap of the cascade with dislocation loops and voids and the consequent change in the overall defect population, CD simulations are performed, and a comparison is made between the cases with overlap events and no overlap events. Figures 10(*a*)–(*d*) illustrate the loop and void density distributions at 400 °C and 600 °C at 1 dpa, while figures 11(*a*)–(*d*) present the evolution of loops as a function of the irradiation dose. The variation in loop density during cascade overlap is influenced by two key factors: (i) during a full cascade overlap, a fraction of the <100> loops transform into smaller <100> and $^1/_2$<111> loops, while a fraction of the $^1/_2$<111> loops also transform into <100> and $^1/_2$<111> loops. These transformations are quantified using transformation coefficients, as detailed in section 3.3. It is important to note that the fraction of $^1/_2$<111> loops formed through cascade overlap with $^1/_2$<111> and <100> loops is higher compared to the fraction of <100> loops formed, and these fractions are taken from the study of Byggmastar *et al* [70]; (ii) The interactions between $^1/_2$<111> and <100> loops lead to coalescence, which results in changes in the overall loop densities.

At both 400 °C and 600 °C, cascade overlap results in an increased distribution of $^1/_2$<111> and <100> loops. Specifically, at 400 °C, the $^1/_2$<111> loop density increases from 8×10^{15} cm^{-3} to 1×10^{16} cm^{-3} (approximately 20%) at 1 dpa, whereas the <100> loop density decreases from 2×10^{15} cm^{-3} to 3×10^{15} cm^{-3} (approximately 33%),

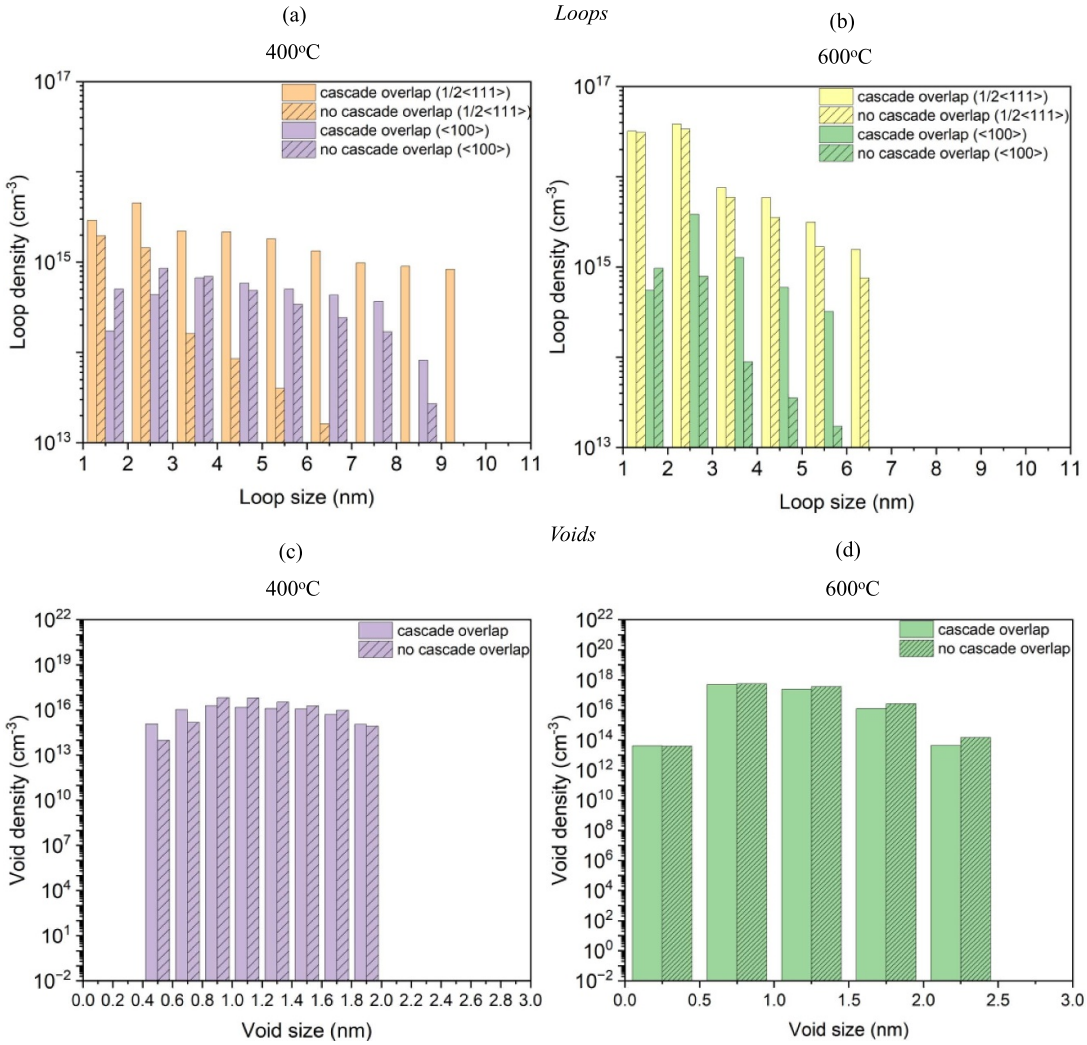

Figure 10. Influence of loop density vs loop size from CD model due to cascade overlap at (*a*) 400 °C and (*b*) 600 °C for 1.02 dpa. Influence of void density vs void size from CD model due to cascade overlap at (*c*) 400 °C and (*d*) 600 °C for 1.02 dpa.

as depicted in figures 10(*a*), 11(*a*) and (*c*). The increase in $^1/_2$<111> loop size and density is primarily driven by the absorption of smaller $^1/_2$<111> loops and <100> loops formed during cascade overlap. The average size of loops is higher in the event of cascade overlap (figure 11(*b*)). The size of the <100> loops increases through the absorption of smaller $^1/_2$<111> loops and mobile SIAs (⩽3). Consequently, the nucleation of new <100> loops leads to an increase in their density (figure 11(*a*)). However, because some of the <100> loops have already been transformed into smaller <100> or $^1/_2$<111> loops, this transformation causes a net increase in the <100> loop density. Moreover, due to the higher population of $^1/_2$<111> loops compared to <100> loops, migrating SIAs and smaller $^1/_2$<111> loops are more likely to be absorbed by $^1/_2$<111> loops than by <100> loops. At a higher temperature of 600 °C, the increase in $^1/_2$<111> loop density is observed during overlap (figures 10(*b*) and 11(*a*), (*c*)). Furthermore, the formation of $^1/_2$<111> and <100> loops derived from the transformation of $^1/_2$<111> loops is higher at 600 °C due to the higher initial $^1/_2$<111> loop density. These smaller <100> loops are subsequently absorbed by $^1/_2$<111> loops, leading to a higher $^1/_2$<111> loop density compared to that under no-overlap conditions. Additionally, the coalescence of smaller $^1/_2$<111> loops with larger <100> loops contributes to an increased <100> loop population under cascade overlap conditions. Since there is an increase in the loop densities during cascade overlap, the number of migrating SIAs is lower for c15 clusters. Therefore, the ratio of SIAs in c15 clusters to SIAs in loops is lower for cascade overlap events when compared to no cascade overlap events (figure 11(*d*) at 400 °C and 600 °C). In the case of voids, there is an overall decrease in the void density at 400 °C and 600 °C (figures 10(*c*) and (*d*)). This is attributed to the fact that the migrating SIAs and $^1/_2$<111> loops formed during the cascade overlap event interact and recombine with the voids, thus reducing the void density.

3.6. Influence on loops and voids due to trapped elements

Figure 12 depicts the $^1/_2$<111> loop, <100> loop and void density distributions for irradiation temperatures of 400 °C and 600 °C. The results demonstrate the comparison between

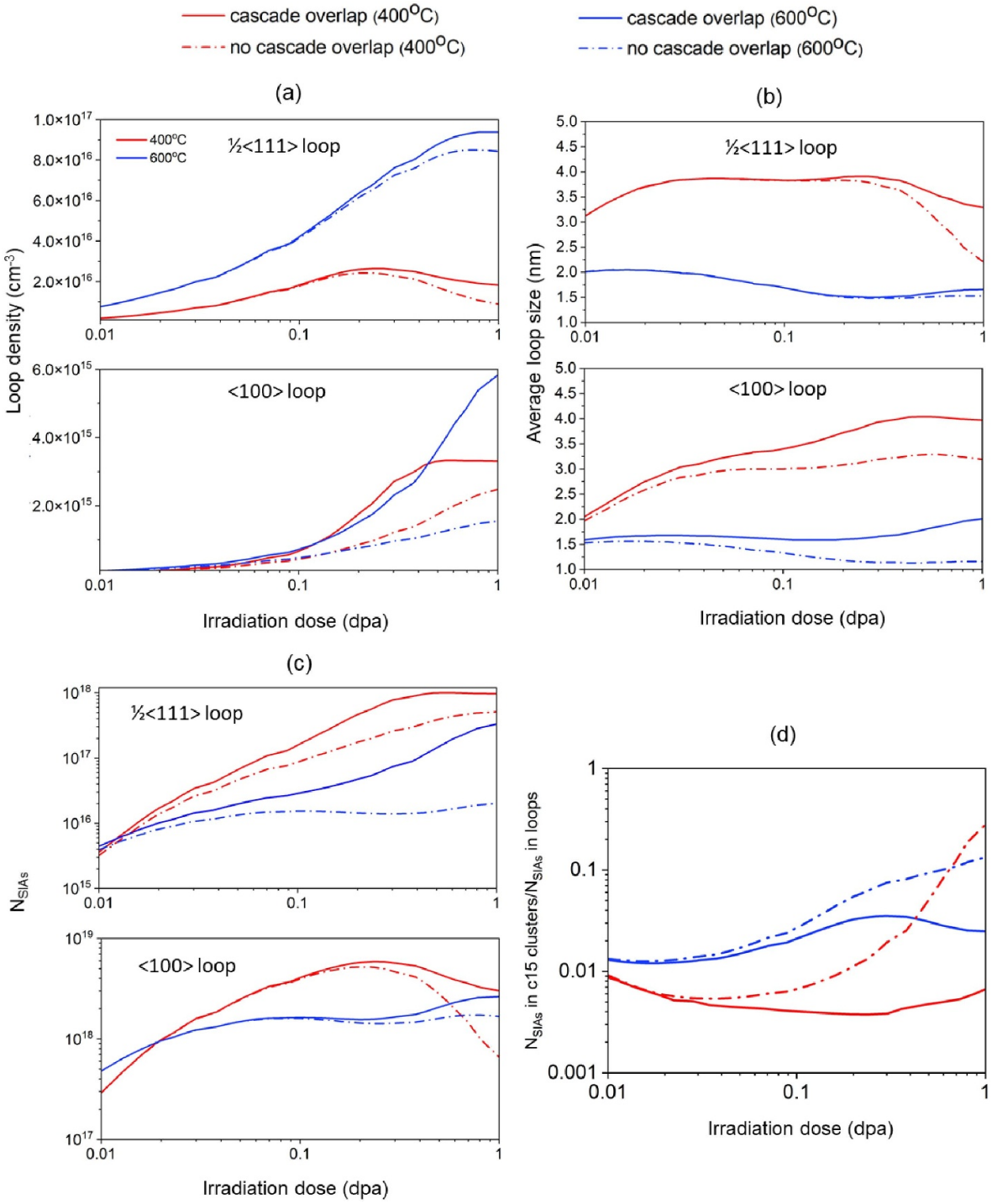

Figure 11. CD model results as a function of irradiation dose (dpa) for (*a*) $^1/_2$<111 > and <100> density; (*b*) average loop size; (*c*) SIAs in $^1/_2$<111> and <100> (in cm^{-3}); (*d*) ratio between SIAs in c15 clusters and SIAs in $^1/_2$<111> and <100 >.

the presence (with traps) and absence (without traps) of the trapped elements. It is obvious from figure 12 that in the presence of interstitial impurity and substitutional transmuted elements, a higher density and size distribution of $^1/_2$<111> loops are observed [17], which are trapped by the interstitial and transmuted elements. In the case without the inclusion of the trap elements, the $^1/_2$<111> loop density distribution is smaller. Due to the high mobility of $^1/_2$<111> loops in W, some of the $^1/_2$<111> loops during their long-range movement are absorbed at sinks (grain boundaries, dislocation line, surface), and most of the remaining $^1/_2$<111> loops are absorbed by <100> loops. In the case of <100> loops, their density and size in the absence of trap elements are lower than in the case with the presence of trap elements. However, a higher density and size of <100> loops are obtained in the presence of trap elements when compared to $^1/_2$<111> loops.

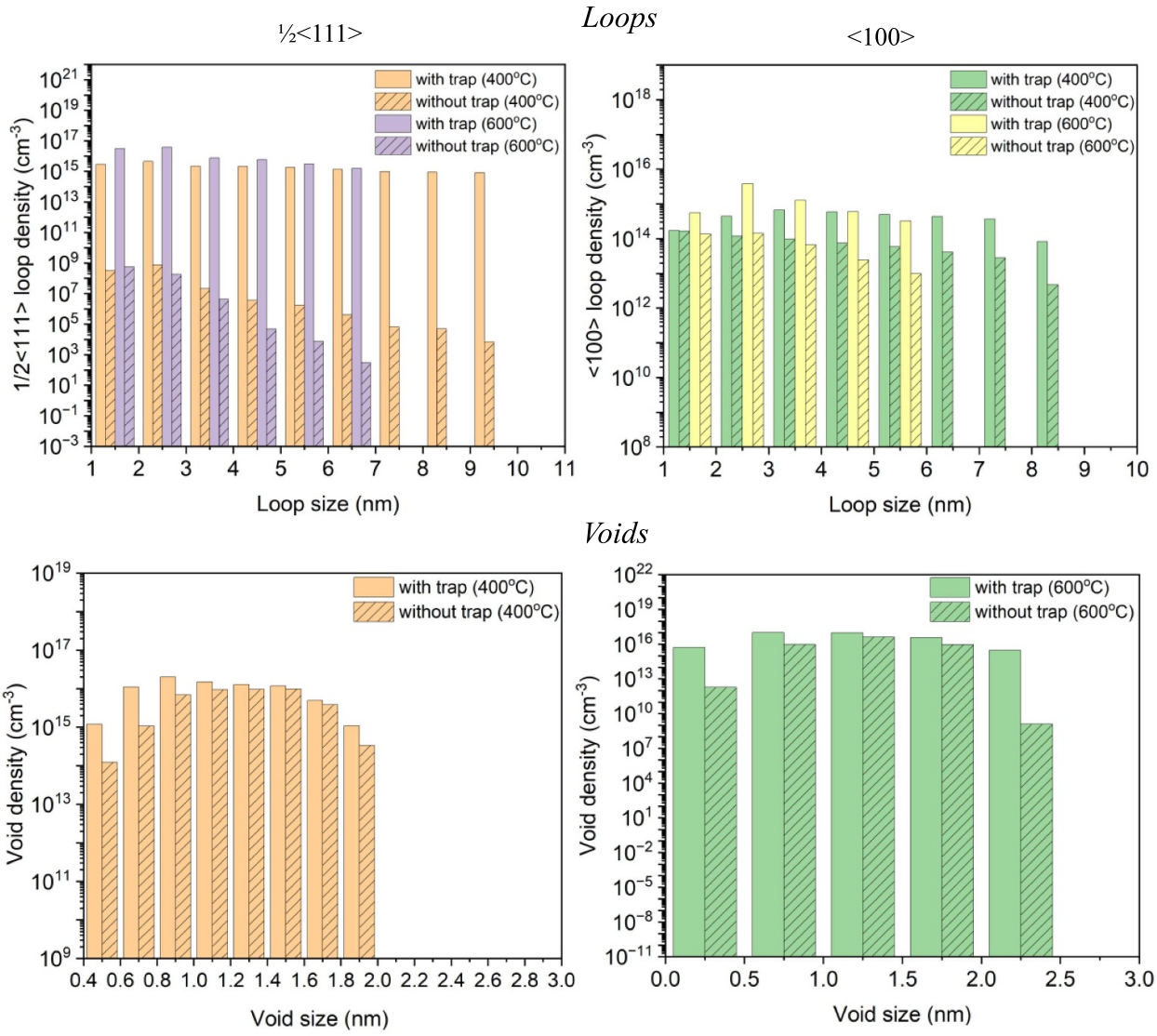

Figure 12. Influence due to trapped elements on $^1/_2$<111> and <100> loop density from CD model for 1.02 dpa (top); influence due to trapped elements on void density from CD model for 1.02 dpa (bottom).

This is due to the fact that, as mentioned before, most of the $^1/_2$<111> loops are subsumed by <100> loops. It is interesting to note that in the presence of trap elements, most of the mobile $^1/_2$<111> loops are impeded by the presence of traps. Therefore, their coalescence with voids is reduced, and a higher density and size of voids is noed. In the case without trap elements, the high mobility of $^1/_2$<111> loops gives them the possibility to coalesce with voids, which leads to a reduction in the density and size of voids when compared to the case with the interaction of $^1/_2$<111> loops with traps. A similar scenario is also noted at the temperature of 600 °C.

Since the $^1/_2$<111> loop density is lower when there are no trap elements, it is expected to have a very low <100> loop density. The source of <100> formation comes from irradiation cascades and cascade overlap events. A fraction of the $^1/_2$<111> loops are transformed to <100> loops during the cascade overlap events and the <100> loop size and density varies based on the coalescence of smaller $^1/_2$<111> loop clusters with <100> loops. In order to understand the number of <100> loops formed by the coalescence of smaller $^1/_2$<111> loop clusters with <100> loops, CD analysis is carried out, not taking into account the reaction between $^1/_2$<111> loops and <100> loops (reaction 'off'). The results obtained from reaction 'off' conditions are compared against reaction 'on' (considering the $^1/_2$<111> and <100> reaction) as shown in figure 13. It is clear from figure 13 that there is a decrease in the <100> loop population under reaction 'off' conditions, which corroborates the fact that the reaction between $^1/_2$<111> and <100> loops promotes an increase in the population of loops of both types ($^1/_2$<111>, <100>).

Figures 14(*a*) and (*b*) illustrate the fraction of interstitials accommodated by sinks (grain boundaries, dislocation network, surface), c15 clusters and loops ($^1/_2$<111> and <100>) as a function of the irradiation dose and temperature, both in the presence and absence of traps. Additionally, loop sizes are shown in figures 14(*c*) and (*d*). Notably, the fraction of SIAs

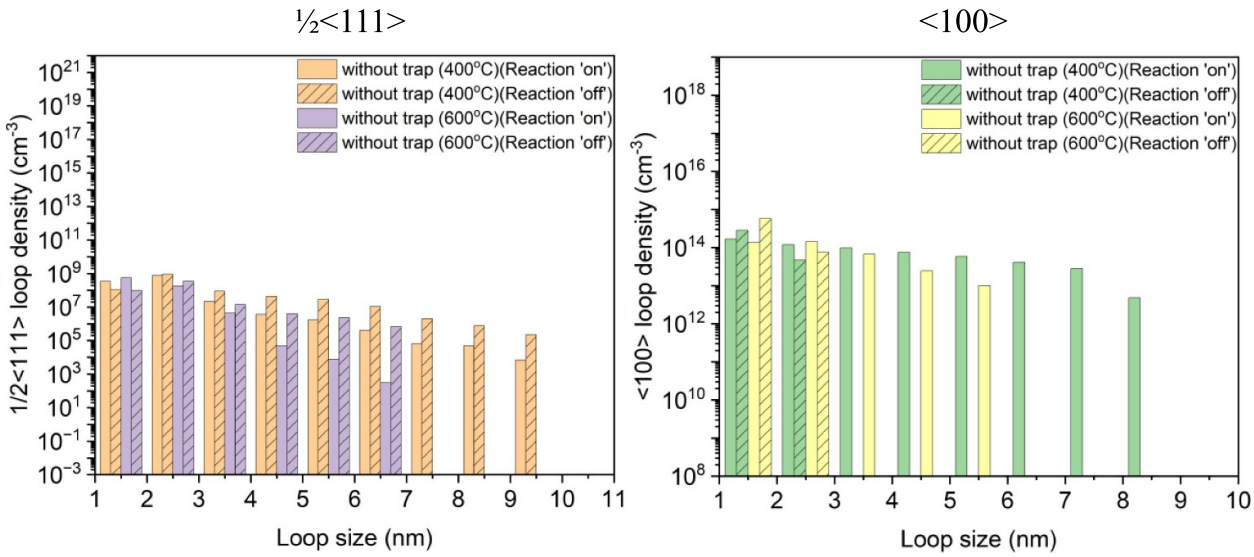

Figure 13. ½<111> (left) and <100> (right) loop density from CD model for reaction 'off' and reaction 'on' conditions. (Reaction 'on' condition refers to reaction between ½<111> and <100> loops, reaction 'off' condition refers to no reaction between ½<111> and <100> loops).

accommodated by ½<111> loops is significantly higher in the presence of traps compared to the case without traps. This occurs because the number of mobile defects available for sink absorption is less when traps are present. However, in the absence of traps, the fraction of interstitials of ½<111> loops decreases after approximately 0.0005 dpa, as most of the SIAs in ½<111> loops are absorbed by sinks and <100> loops (figures 14(*a*) and (*b*)) [76]. In the absence of traps, the high mobility of ½<111> loops causes their size to increase during the early stages of evolution (up to 0.0005–0.001 dpa) (figure 14(*c*)). However, beyond this point, their absorption by sinks and <100> loops leads to a gradual decrease in their size, while <100> loops continue to grow until ∼0.01 dpa (figure 14(*d*)) [75]. As the irradiation progresses, the number of smaller ½<111> loops declines due to their high mobility, leading to absorption at sinks and interaction with <100> loops. This reduction in available SIAs slows the conversion of ½<111> loops into <100> loops, ultimately resulting in a decline in the <100> loop size (figure 14(*d*)).

3.7. Influence of loop reaction

In order to understand the influence of ½<111> loop and <100> loop interaction on the overall defect population in W material, simulations are performed for reaction 'on' and reaction 'off' conditions. Reaction 'on' corresponds to the reaction between the ½<111> and <100> loops, while reaction 'off' does not take into account the interaction between ½<111> and <100> loops. Figure 15 depicts the loop and void density distribution in reaction 'on' and reaction 'off' conditions. Figures 16(*a*) and (*b*) depict the ratio between SIAs in ½<111> and SIAs in <100> loops, and figure 16(*b*) depicts the ratio of the number of SIAs in c15 clusters to the number of SIAs in loops. To analyze the density of c15 clusters, the ratio between SIAs in c15 clusters and SIAs in ½<111> + <100> loops is also evaluated, as shown in figure 16(*b*).

For irradiation temperatures of 400 °C and 600 °C, the density distribution of ½<111> loops is higher in the reaction 'off' condition when compared to the reaction 'on' condition, as shown in figure 15. The density decreasing in the reaction 'on' condition is attributed to the reaction between ½<111> loops and <100> loops, while reaction 'off' means not taking into account the interaction between ½<111> loops and <100> loops. At an irradiation temperature of 400 °C under reaction 'off' conditions, a higher <100> loop density is observed for a loop size less than 3 nm when compared to reaction 'on' conditions. However, at a loop size greater than 3 nm, no <100> loops are observed for the reaction 'off' case. In the case of 600 °C, a higher <100> loop density is noted at loop sizes less than 3 nm for reaction 'off' conditions compared with reaction 'on' conditions. A similar trend is observed for ½ <111> loops, which shows that for the reaction 'on' condition, the interaction between ½<111> and <100> loops promotes the growth of <100> loops (figures 15(*a*) and (*b*)). It is quite obvious from figures 15(*c*) and (*d*) that a lower density of voids is observed in the reaction 'off' condition at temperatures of 400 °C and 600 °C at a size greater than 1 nm since the SIAs from loops coalesce with the vacancies. At 400 °C, in the absence of ½<111> and <100> loop interactions (reaction 'off' condition), the reduced vacancy diffusivity at this temperature compared to 600 °C limits vacancy recombination and the coalescence of vacancy clusters into larger voids, leading to an overall increase in small void formation (<0.6 nm) (figure 15(*c*)). Furthermore, since the population of ½<111> loops is lower under the reaction 'off' condition compared to the reaction 'on' condition, the total absorption of mobile vacancies (⩽4) by loops is reduced. As

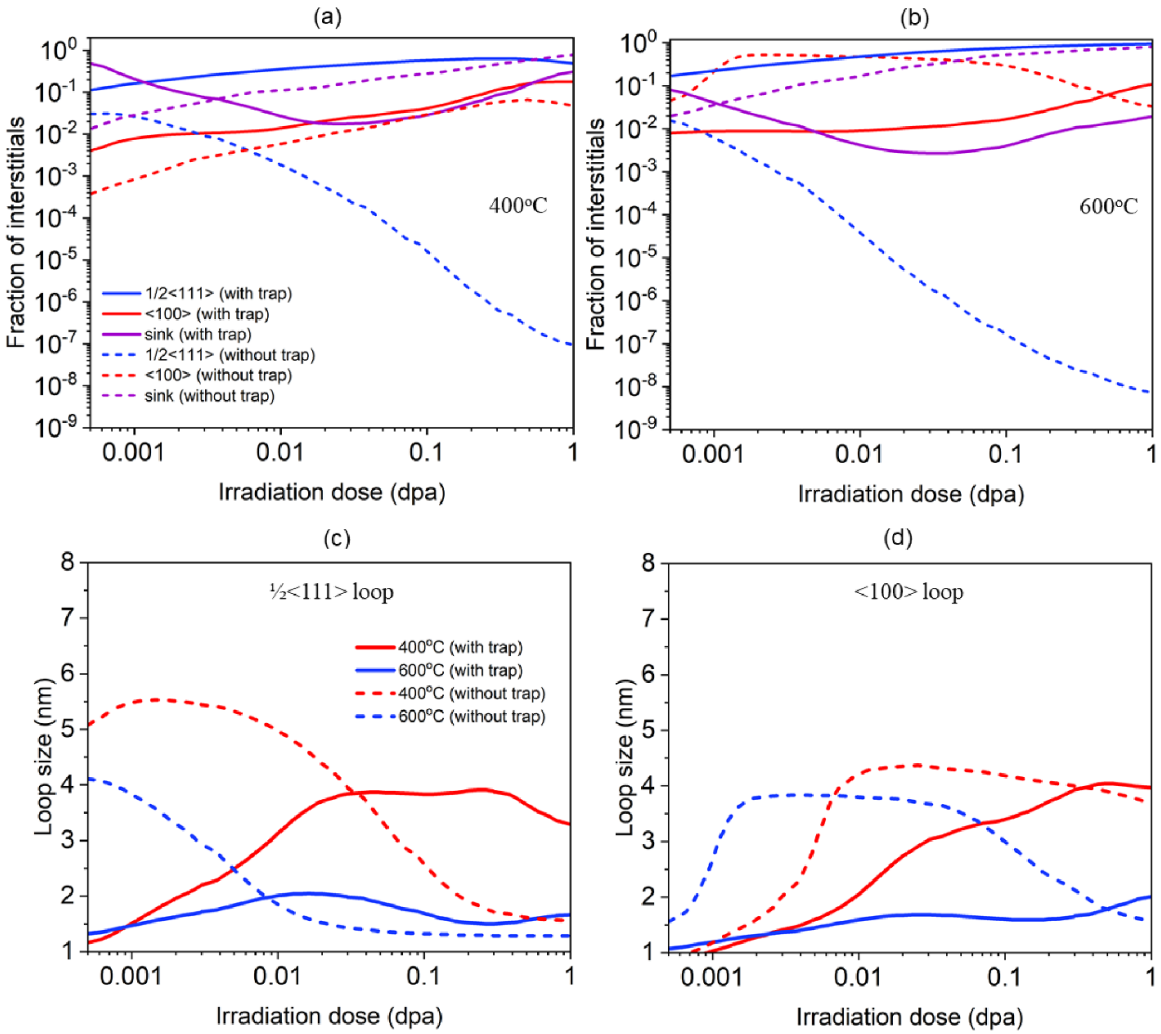

Figure 14. CD model results as a function of irradiation dose (dpa) for SIAs in $^1/_2$<111> and <100> at (*a*) 400 °C, (*b*) 600 °, (*c*) $^1/_2$ <111> loop size, (*d*) <100> loop size.

a result, more vacancies remain available to cluster into small voids (⩽0.5 nm), further contributing to their higher density under the reaction 'off' condition.

At 600 °C, the suppression of small voids (<0.5 nm) under the reaction 'off' condition can be attributed to two key factors. Firstly, the higher diffusivity of vacancies (⩽4) at this elevated temperature allows them to migrate and contribute to the growth of larger voids but with lower density compared to the reaction 'on' condition (figure 15(*d*)). Secondly, the higher $^1/_2$<111> loop population in the reaction 'off' condition at 600 °C compared to 400 °C enhances vacancy absorption (⩽4), which consequently leads to a greater reduction in the number of vacancies available for small void nucleation. As a result, the formation of small voids is suppressed.

The N_{SIAs} accommodated by the $^1/_2$<111> and <100> loops are evaluated based on the ratio between SIAs in the $^1/_2$<111> and <100> loops (figure 16(*a*)). Under the reaction 'on' condition, the reaction between $^1/_2$<111> and <100> loops promotes $^1/_2$<111> and <100> loop growth by accommodating N_{SIAs} by both types of loops. In fact, the number of SIAs gained by <100> loops is higher with respect to $^1/_2$<111> loops and, therefore, a decrease in the ratio between SIAs gained by $^1/_2$<111> and <100> loops is observed as a function of the irradiation dose at both irradiation temperatures. However, under reaction 'off' conditions, at 400 °C and 600 °C, there is an overall reduction in the <100> loop population due to the absence of reactions between the $^1/_2$<111> and <100> loops for the growth of loops. This leads to an increase in the ratio of N_{SIAs} in reaction 'off' conditions compared with reaction 'on' conditions. Since there is no transfer of SIAs between $^1/_2$<111> and <100> loops under reaction 'off' conditions, more SIAs are accommodated in the c15 clusters with respect to the reaction 'on' condition (figure 16(*b*). Moreover, at higher temperatures, fewer SIAs are accommodated by loops than c15 clusters. The density of voids is influenced by the SIAs involved in the formation of the

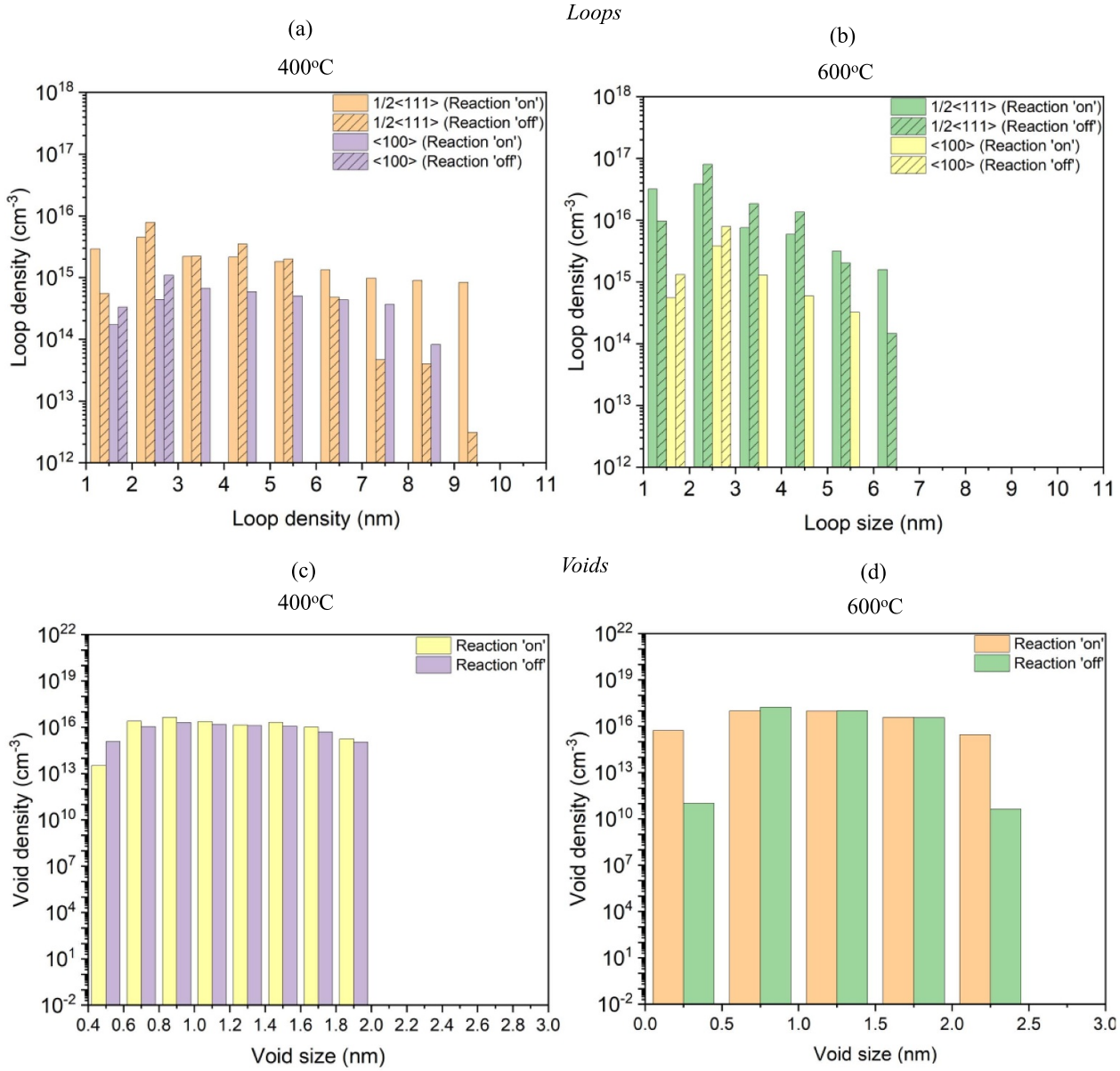

Figure 15. Influence of loop density vs loop size from CD model due to reaction conditions between $^1/_2$<111> and <100> loops at (*a*) 400 °C and (*b*) 600 °C for 1.02 dpa. Influence of void density vs void size from CD model due to reaction conditions between $^1/_2$<111> and <100> loops at (*c*) 400 °C and (*d*) 600 °C for 1.02 dpa. (Reaction 'on' condition refers to reaction between $^1/_2$<111> and <100> loops, reaction 'off' condition refers to no reaction between $^1/_2$<111> and <100> loops).

loops. Since there is no transfer of SIAs between $^1/_2$<111> and <100> loops, most of the SIAs will either be absorbed by c15 clusters or voids.

4. Discussions

There are several mechanisms involved in the formation of <100> loops in irradiated W. One such mechanism for the formation of <100> loops is the interaction between $^1/_2$<111> loops of identical size. However, such reactions are rare. Since the formation energy of $^1/_2$<111> loops is lower than that of <100> loops, the probability of the formation of <100> loops is lower with respect to the formation of $^1/_2$<111> loops [15]. The model has considered a probability of ∼3/8 for the formation of <100> loops resulting from the reaction between $^1/_2$<111> loops of the same size, but the proportion of <100> loops formed through this interaction is much less in the present study. Therefore, in the current model, the main source for the formation of <100> loops is the generation directly in irradiation cascades and full cascade overlap with pre-existing defects. The density of $^1/_2$<111> loops is found to be higher than that of <100> loops at various irradiation temperatures. The formation of $^1/_2$<111> loops and <100> loops by means of c15 cluster collapse is not considered in this study since the irradiation temperature employed in the experimental and numerical study is not sufficient for the collapse of c15 clusters in W, as explained in the

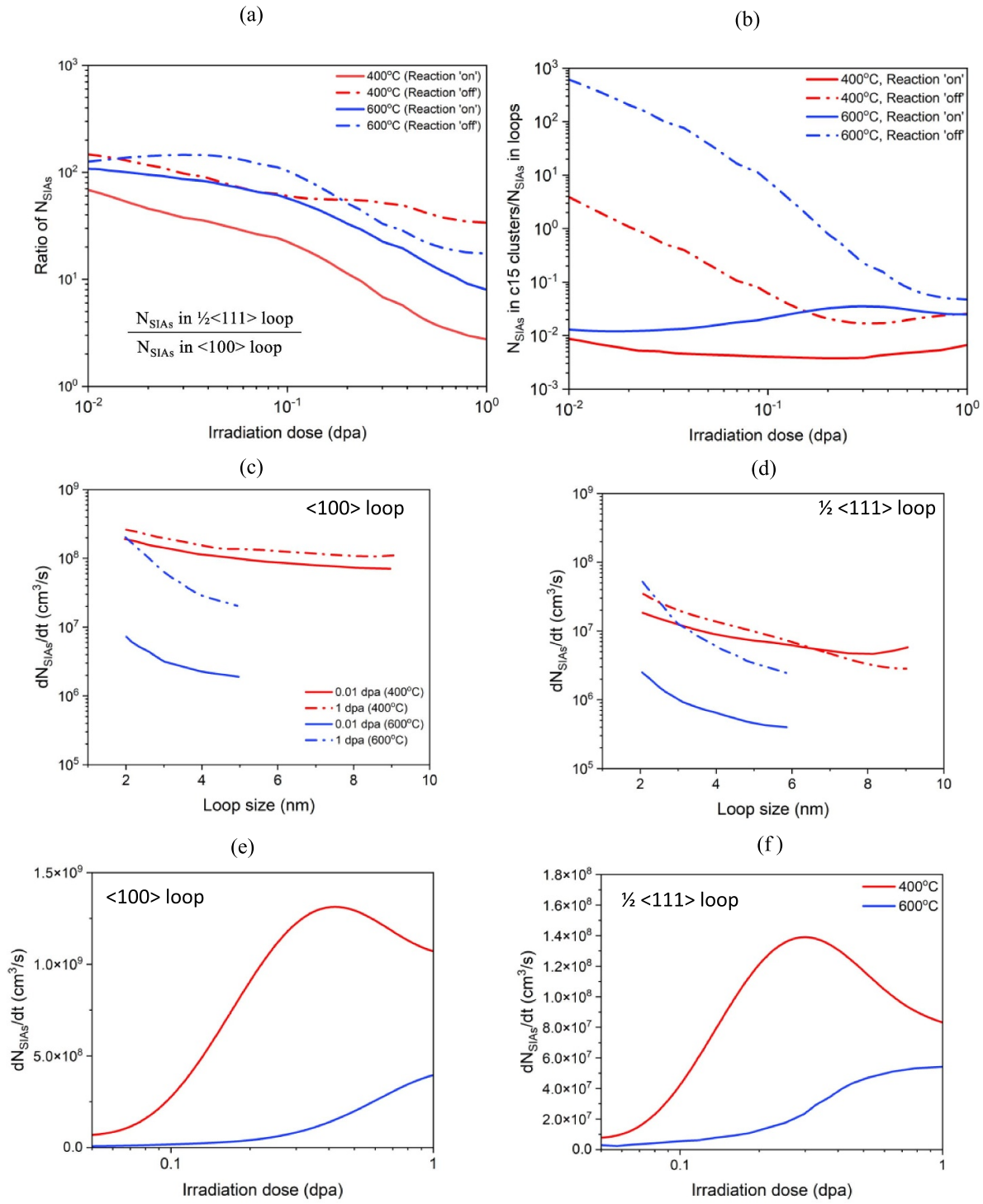

Figure 16. CD model results for (*a*) ratio between SIAs in $^1/_2$<111> and <100>; (*b*) ratio between SIAs in c15 clusters and SIAs in $^1/_2$<111> and <100>; (*c*) SIA transfer rate to <100> loop; (*d*) SIA transfer rate to $^1/_2$<111> loop; (*e*) total SIA transfer rate of <111> loop to form <100> loop; (*f*) total SIA transfer rate of <100> loop to form $^1/_2$<111> loop.

previous work of Liu *et al* [41, 42]. However, there are only a few studies available in the literature regarding the stability of c15 clusters in W, which can influence the long-term evolution of $^1/_2$<111> and <100> density and size.

The temporal evolution of the defect features is influenced by the interaction with the trap elements (impurity atoms + transmuted elements). Due to these interactions, the size and density of loops and voids have an influence on the material behavior, as explained in section 3.6. Since the sample used in this study is a bulk material, the surface effects are not important. Therefore, the highly mobile $^1/_2$<111> loops can be sunk at grain boundaries or be incorporated into dislocation lines. In particular, with the inclusion of the trap elements, the model can capture a higher concentration

of $^1/_2$<111> loops. This kind of scenario is highlighted in the experimental work of Klimenkov *et al* [17]. Moreover, a detailed study is required to include Re atoms in the CD model to understand the long-range interaction of Re atoms with loops and voids.

In order to increase the rate of interaction between $^1/_2$<111> and <100> loops, the influence of the mean free path is relevant, which depends on the population of $^1/_2$<111> and <100> loops. To understand the evolution of the loops at extended irradiation fluence, there is a need to gain some insights into the mutual transfer of SIAs due to the reaction between $^1/_2$<111> and <100> loops. The overall loop population also depends on the reaction between $^1/_2$<111> and <100> loops, which fosters the loop population via absorption or coalescence reactions. In fact, the change in the loop population results in SIA transfer between the loops and influences the SIAs in the loops with respect to their initial microstructure. The SIA transfer rate between the $^1/_2$<111> and <100> loops is studied based on a similar approach to that used by Gao *et al* [45], and the expressions for the SIA transfer rate for $^1/_2$<111> and <100> loops are calculated as follows in equations (26) and (27):

$$\mathrm{Tran}_{111}(j) = \sum_{j>i} k_i^j C_{111}(j)\, C_{100}(i)\, .i - \sum_{j<i'} k_{i'}^j C_{111}(j)\, C_{100}(i')\, .j \tag{26}$$

$$\mathrm{Tran}_{100}(j) = \sum_{j>i} k_i^j C_{100}(j)\, C_{111}(i)\, .i - \sum_{j<i'} k_{i'}^j C_{100}(j)\, C_{111}(i')\, .j. \tag{27}$$

The SIAs received by $^1/_2$<111> loops by absorbing the smaller loop size of <100> type are depicted in the $k_i^j C_{111}(j)\, C_{100}(i)\, .i$ term, while the $k_{i'}^j C_{111}(j)\, C_{100}(i')\, .j$ term depicts the <100> loop of larger size absorbing the smaller loop size $^1/_2$<111> type. A positive value of $\mathrm{Tran}_{111}(j)$ depicts the gain of SIAs by $^1/_2$<111 > of size j from <100> loops through the '$^1/_2$<111>+ <100>' reaction. In the case of negative $\mathrm{Tran}_{111}(j)$, there is a loss of SIAs from the $^1/_2$<111> loop. The terms in equations (26) and (27) have a similar depiction for <100> loops.

Figures 16(*c*) and (*d*) depict the SIA transfer rate to form $^1/_2$<111> and <100> loops. It is worthwhile to note that in general both $^1/_2$<111> and <100> loops gain SIAs due to their reaction due to the positive Tran_{111} and Tran_{100}, which corroborates the fact that the SIA transfer promotes the variation in the loop densities of $^1/_2$<111> and <100>. The rate at which the SIAs are gained by the <100> loop is higher with respect to the $^1/_2$<111> loop at both irradiation temperatures (400 °C and 600 °C). <100> loops achieve a larger gain of SIAs due to the higher production of smaller $^1/_2$<111> loops as a result of SIA aggregation and in-cascade clustering. In particular, SIAs gained by <100> loops increase with the dose at 400 °C. However, at 600 °C, the amount of SIAs gained by <100> loops is lower compared with that at the irradiation temperature of 400 °C. Therefore, the ratio of SIAs in $^1/_2$<111> loops to <100> loops is higher at 600 °C. The lower density of the higher sized loops ($^1/_2$<111>, <100>) is due to the low transfer rate of SIAs. Moreover, with the increase in the irradiation dose, the SIAs gained by the $^1/_2$<111> loop are decreased. For this reason, the reduction in SIA gain of $^1/_2$<111> loops promotes an increase in gain in SIAs for <100> loops. The total SIA transfer rates, obtained by summing the contributions from the $^1/_2$<111> and <100> loops, offer valuable insights into the mechanisms driving loop evolution under irradiation (figures 16(*e*) and (*f*)). At 400 °C, the transfer of SIAs from $^1/_2$<111> loops to <100> loops increases up to 0.2 dpa due to the progressive absorption of smaller $^1/_2$<111> loops by larger <100> loops. This redistribution of SIAs supports the continued growth of <100> loops in the early stages of irradiation. Beyond 0.2 dpa, the SIA transfer rate declines, mainly due to interacting defect mechanisms. As the irradiation dose increases, vacancy accumulation and recombination with mobile SIAs reduce the overall availability of SIAs for loop absorption. Additionally, the absorption of SIAs by sinks such as grain boundaries and dislocation networks further limits their contribution to loop growth. A similar trend is observed for the transfer of SIAs from <100> loops to $^1/_2$<111> loops over 0.2 dpa, but the magnitude of this transfer is lower than that from $^1/_2$<111> loops to <100> loops. Since the primary mechanism of loop evolution is the absorption of $^1/_2$<111> loops by <100> loops, the reduced availability of SIAs limits the transfer from <100> loops to $^1/_2$<111> loops. At 600 °C, the increased mobility of SIAs at this temperature, compared to 400 °C, enhances loop absorption, resulting in a higher transfer rate of SIAs from $^1/_2$<111> loops to <100> loops up to approximately 1 dpa (figures 16(*e*) and (*f*)). Moreover, at higher doses, accelerated vacancy diffusion promotes faster recombination between SIAs and vacancies, reducing the net availability of mobile SIAs. As a result, the rate of SIA transfer from <100> to $^1/_2$<111> loops is less at around 1 dpa as recombination with vacancies and defect sinks becomes increasingly significant.

5. Conclusions

Neutron irradiation-induced defects pose the main challenge in the design and development of in-vessel components in fusion reactors due to alteration of the material properties. Moreover, studies addressing the behavior of W-based components in fusion-relevant conditions are still ongoing. In order to understand the microstructural evolution of irradiation-induced defects in W, the present study included an integrated experimental–numerical analysis on neutron-irradiated W. Regarding the experimental analysis, TEM characterization was carried out for W irradiated up to 1 dpa at 400 °C and 600 °C. The CD method, developed in this study, was employed to investigate the long-term evolution of $^1/_2$<111> loops, <100> loops, voids and c15 clusters by

assigning the irradiation conditions implemented for experimental analysis. The numerical results obtained from the CD method are compared with the experimental data. The following statements highlight the findings obtained in this work:

(1) In the CD model developed for W, the evolution of cluster densities (loops/voids) depends on various factors, such as the defect production rate, initial defect production numbers and fraction of loops ($^1/_2$<111>, <100>), voids produced during irradiation cascades, the boundary condition of loops and voids (number of SIAs and vacancies) initialized for the CD computations, the energetics of defect densities (formation energy, migration energy) and the diffusion coefficient of defect densities. The CD results for 400 °C are in good agreement with the experimental results. However, there are larger loops obtained for 600 °C in the CD results, which are not observed in the experimental results. This is a better case scenario that the current study has obtained for 400 °C and 600 °C in the CD model since the relative population of the $^1/_2$<111> and <100> loops at 400 °C and 600 °C follows the same trend as that of the experimental results. Concerning the experimental results, loops of less than 2 nm and black dots are not counted in the TEM analysis at both 400 °C and 600 °C. The types of defects regarding black dots are yet to be verified. As the temperature increases, the formation energy of $^1/_2$<111> loops decreases, requiring less energy for their formation and making them more likely to form than <100> loops. Moreover, the formation energy of $^1/_2$<111> loops remains consistently lower than that of <100> loops. As a result, the density of $^1/_2$<111> loops is expected to be higher than that of <100> loops.
(2) Irradiation cascades overlapping with pre-existing SIA clusters in W contribute to the nucleation of <100> and $^1/_2$<111> dislocation loops, impacting the long-term evolution of defects. The variation in loop density is driven by the formation of <100> and $^1/_2$<111> loops during cascade overlap, which are subsequently absorbed by larger $^1/_2$<111> and <100> loops, thereby modifying their densities. The characteristics of cascade overlap, such as the fraction and type of clusters formed, depend on factors such as the PKA energy and temperature. However, due to the limited availability of cascade overlap data, particularly regarding changes in the fraction and type of pre-existing clusters as a function of temperature, further studies using lower-scale models like MD are necessary. Such data could be valuable for enhancing CD models to better predict defect evolution under varying temperature conditions based on cascade overlap events.
(3) Due to the high mobility of $^1/_2$<111> loops in W, in the absence of traps, most of the $^1/_2$<111> loops are either absorbed at sinks (dislocation lines, grain boundaries, free surfaces) or coalesced with <100> loops and voids, which decreases the overall $^1/_2$<111> loop population, as corroborated in the CD model. With the inclusion of traps, a higher $^1/_2$<111> loop population is noted. The indication of the differences in the $^1/_2$<111> loop density resulting from the influence of traps, however, warrants further detailed investigation focusing on the incorporation of Re/Os atoms and their interaction with $^1/_2$<111> loops and voids in the CD model. On the basis of the current work, our next work will focus on the employment of concentration equations for transmuted elements (Re/Os), transmuted elements–W interstitial clusters and transmuted elements–W vacancy clusters in the CD model to provide more insights on the trapping of mobile $^1/_2$<111> loops and vacancy clusters by the transmuted elements and to understand the consequent influence on defect cluster evolution.
(4) During the long-term evolution of loops, the reaction between $^1/_2$<111> loops and <100> loops was recognized as the source of transfer of SIAs between loops of different Burgers vectors. The reaction facilitates the modification in the loop population of both types. The rate at which SIAs are gained by the <100> loop is higher compared to the $^1/_2$<111> loop. This enhanced SIA gain in <100> loops is attributed to the higher production of smaller $^1/_2$<111> loops, resulting from the accumulation of SIAs and in-cascade clustering. Specifically, for larger <100> loops, the SIA transfer rate decreases with the increase in irradiation dose.

Based on previous studies employing the CD model, a key tenet of the current work is the assessment of the long-term evolution of $^1/_2$<111> loops, <100> loops and voids. The CD model provides accurate predictions of the irradiation-induced microstructure in neutron-irradiated W, including loops, voids and C15 clusters, while incorporating the latest insights into radiation damage evolution and W energetics. The hope is that the parameters and results obtained from this integrated experimental–numerical approach can be useful for providing information for upper-scale models like dislocation dynamics, finite element models for investigating the engineering properties and thermo-mechanical behavior of fusion-relevant components.

Acknowledgment

This work was supported by the Helmholtz Association of German Research Centers (HGF) and carried out within the framework of the Nuclear Fusion Programme at Karlsruhe Institute of Technology (KIT), Germany. The authors would like to thank all the members of the Fusion Materials Laboratory (FML) of KIT for their help in handling irradiated materials.

This work was carried out within the framework of the EUROfusion Consortium, funded by the European Union via the Euratom Research and Training Programme (Grant Agreement No. 101052200—EUROfusion). Views and opinions expressed are however those of the author(s) only and

do not necessarily reflect those of the European Union or the European Commission. Neither the European Union nor the European Commission can be held responsible for them.

CRediT authorship contribution statement

Salahudeen Mohamed: Conceptualization, methodology software, formal analysis, investigation, writing—original draft and visualization. **Qian Yuan:** Resources, investigation, writing—review and editing. **Dimitri Litvinov:** Resources, writing—review and editing. **Jie Gao:** Investigation, software, writing—review and editing. **Ermile Gaganidze:** Investigation, resources, writing—review and editing. **Dmitry Terentyev:** Investigation, writing—review and editing. **Hans-Christian Schneider:** Investigation, writing—review and editing. **Jarir Aktaa:** Investigation, resources, writing—review and editing.

Conflict of interest

The authors declare that they have no known competing financial interests or personal relationships that could have appeared to influence the work reported in this paper.

ORCID iDs

Jie Gao https://orcid.org/0000-0002-4321-4063
Jarir Aktaa https://orcid.org/0000-0002-0891-5331

References

[1] Dudarev S.L. *et al* 2009 The EU programme for modelling radiation effects in fusion reactor materials: an overview of recent advances and future goals *J. Nucl. Mater.* **386–388** 1–7
[2] Federici G., Biel W., Gilbert M.R., Kemp R., Taylor N. and Wenninger R. 2017 European DEMO design strategy and consequences for materials *Nucl. Fusion* **57** 092002
[3] Voitsenya V.S., Balden M., Bardamid A.F., Belyaeva A.I., Bondarenko V.N., Skoryk O.O., Shtan' A.F., Solodovchenko S.I., Sterligov V.A. and Tyburska-Püschel B. 2014 Effect of sputtering on self-damaged ITER-grade tungsten *J. Nucl. Mater.* **453** 60–65
[4] Dellis S., Xiao X., Terentyev D., Mergia K., Krimpalis S., Bakaev A. and Messoloras S. 2021 Mechanical properties of neutron-irradiated single crystal tungsten W(100) studied by indentation and FEM modeling *J. Nucl. Mater.* **551** 152985
[5] Dai C., Wang Q., Saidi P., Langelier B., Judge C.D., Daymond M.R. and Mattucci M.A. 2022 Atomistic structure and thermal stability of dislocation loops, stacking fault tetrahedra, and voids in face-centered cubic Fe *J. Nucl. Mater.* **563** 153636
[6] Terentyev D. *et al* 2022 Recent progress in the assessment of irradiation effects for in-vessel fusion materials: tungsten and copper alloys *Nucl. Fusion* **62** 026045
[7] Linke J., Du J., Loewenhoff T., Pintsuk G., Spilker B., Steudel I. and Wirtz M. 2019 Challenges for plasma-facing components in nuclear fusion *Matter Radiat. Extremes* **4** 056201
[8] Gilbert M.R., Dudarev S.L., Nguyen-Manh D., Zheng S., Packer L.W. and Sublet J.-C. 2013 Neutron-induced dpa, transmutations, gas production, and helium embrittlement of fusion materials *J. Nucl. Mater.* **442** S755–60
[9] Pintsuk G. 2012 Tungsten as a plasma-facing material *Comprehensive Nuclear Materials* **4** 551–81
[10] Gaganidze E., Chauhan A., Schneider H.-C., Terentyev D., Rossaert B. and Aktaa J. 2021 Effect of irradiation temperature on the fracture-mechanical behaviour of tungsten irradiated to 1 dpa *J. Nucl. Mater.* **556** 153200
[11] Gavila P., Riccardi B., Constans S., Jouvelot J.L., Vastra I.B., Missirlian M. and Richou M. 2011 High heat flux testing of mock-ups for a full tungsten ITER divertor *Fusion Eng. Des.* **86** 1652–5
[12] Dürrschnabel M., Klimenkov M., Jäntsch U., Rieth M., Schneider H.C. and Terentyev D. 2021 New insights into microstructure of neutron-irradiated tungsten *Sci. Rep.* **11** 7572
[13] Klimenkov M., Jäntsch U., Rieth M., Schneider H.C., Terentyev D. and Van Renterghem W. 2024 Influence of transmutation-induced Re/Os content on defect evolution in neutron-irradiated W *J. Nucl. Mater.* **592** 154950
[14] Yi X., Jenkins M.L., Briceno M., Roberts S.G., Zhou Z. and Kirk M.A. 2013 *In situ* study of self-ion irradiation damage in W and W–5Re at 500 °C *Phil. Mag.* **93** 1715–38
[15] Li Y. *et al* 2021 In-situ TEM investigation of 30 keV he+ irradiated tungsten: effects of temperature, fluence, and sample thickness on dislocation loop evolution *Acta Mater.* **206** 116618
[16] Chauhan A., Yuan Q., Litvinov D., Gaganidze E., Schneider H.-C., Terentyev D. and Aktaa J. 2022 Effect of temperature on the neutron irradiation-induced cavities in tungsten *Phil. Mag.* **102** 1665–83
[17] Klimenkov M., Dürrschnabel M., Jäntsch U., Lied P., Rieth M., Schneider H.C., Terentyev D. and Van Renterghem W. 2022 Microstructural analysis of W irradiated at different temperatures *J. Nucl. Mater.* **572** 154018
[18] Zheng R.-Y. and Han W.-Z. 2020 Comparative study of radiation defects in ion irradiated bulk and thin-foil tungsten *Acta Mater.* **186** 162–71
[19] El-Atwani O., Cunningham W.S., Trelewicz J.R., Li M., Wirth B.D. and Maloy S.A. 2020 Revealing the synergistic effects of sequential and simultaneous dual beam irradiations in tungsten via in-situ TEM *J. Nucl. Mater.* **538** 152150
[20] Harrison R.W., Peng N., Webb R.P., Hinks J.A. and Donnelly S.E. 2019 Characterisation of helium ion irradiated bulk tungsten: a comparison with the in-situ TEM technique *Fusion Eng. Des.* **138** 210–6
[21] Harrison R.W., Greaves G., Hinks J.A. and Donnelly S.E. 2017 A study of the effect of helium concentration and displacement damage on the microstructure of helium ion irradiated tungsten *J. Nucl. Mater.* **495** 492–503
[22] Harrison R.W., Amari H., Greaves G., Hinks J.A. and Donnelly S.E. 2016 Effect of He-appm/DPA ratio on the damage microstructure of tungsten *MRS Adv.* **1** 2893–9
[23] Sand A.E., Dudarev S.L. and Nordlund K. 2013 High-energy collision cascades in tungsten: dislocation loops structure and clustering scaling laws *EPL Europhys. Lett.* **103** 46003
[24] Yi X., Jenkins M.L., Kirk M.A., Zhou Z. and Roberts S.G. 2016 In-situ TEM studies of 150 keV W+ ion irradiated W and W-alloys: damage production and microstructural evolution *Acta Mater.* **112** 105–20
[25] English C.A. and Jenkins M.L. 2010 Molecular ion irradiations of molybdenum *Phil. Mag.* **90** 821–43
[26] Sand A.E., Mason D.R., De Backer A., Yi X., Dudarev S.L. and Nordlund K. 2017 Cascade fragmentation: deviation from power law in primary radiation damage *Mater. Res. Lett.* **5** 357–63

[27] Castin N., Bakaev A., Bonny G., Sand A.E., Malerba L. and Terentyev D. 2017 On the onset of void swelling in pure tungsten under neutron irradiation: an object kinetic Monte Carlo approach *J. Nucl. Mater.* **493** 280–93

[28] Zhao Z., Li Y., Zhang C., Pan G., Tang P. and Zeng Z. 2017 Effect of grain size on the behavior of hydrogen/helium retention in tungsten: a cluster dynamics modeling *Nucl. Fusion* **57** 086020

[29] Li Y.G., Zhou W.H., Huang L.F., Zeng Z. and Ju X. 2012 Cluster dynamics modeling of accumulation and diffusion of helium in neutron irradiated tungsten *J. Nucl. Mater.* **431** 26–32

[30] Krasheninnikov S.I., Faney T. and Wirth B.D. 2014 On helium cluster dynamics in tungsten plasma facing components of fusion devices *Nucl. Fusion* **54** 073019

[31] Shah V., Van Dommelen J.A.W. and Geers M.G.D. 2020 Spatially dependent kinetics of helium in tungsten under fusion conditions *J. Nucl. Mater.* **535** 152104

[32] Faney T., Krasheninnikov S.I. and Wirth B.D. 2015 Spatially dependent cluster dynamics model of He plasma surface interaction in tungsten for fusion relevant conditions *Nucl. Fusion* **55** 013014

[33] Xiong Y., Huang S., Zhang J., Ma S., Xu B., Fu H., Xiang X., Lu W. and Zhao S. 2024 A review of cluster dynamics in studying radiation damage: dominant factors and practical implications *JOM* **76** 5785–802

[34] Hu X., Xu D. and Wirth B.D. 2013 Quantifying He-point defect interactions in Fe through coordinated experimental and modeling studies of He-ion implanted single-crystal Fe *J. Nucl. Mater.* **442** S649–54

[35] Faney T. and Wirth B.D. 2014 Spatially dependent cluster dynamics modeling of microstructure evolution in low energy helium irradiated tungsten *Modelling Simul. Mater. Sci. Eng.* **22** 065010

[36] Kohnert A.A. and Wirth B.D. 2015 Cluster dynamics models of irradiation damage accumulation in ferritic iron. I. Trap mediated interstitial cluster diffusion *J. Appl. Phys.* **117** 154305

[37] Sand A.E., Aliaga M.J., Caturla M.J. and Nordlund K. 2016 Surface effects and statistical laws of defects in primary radiation damage: tungsten vs. iron *EPL Europhys. Lett.* **115** 36001

[38] Shen H., Nutt S. and Hull D. 2004 Direct observation and measurement of fiber architecture in short fiber-polymer composite foam through micro-CT imaging *Compos. Sci. Technol.* **64** 2113–20

[39] Mannheim A., Van Dommelen J.A.W. and Geers M.G.D. 2018 Modelling recrystallization and grain growth of tungsten induced by neutron displacement defects *Mech. Mater.* **123** 43–58

[40] Wei L., Zhang C., Zheng Q., Zeng Z. and Li Y. 2022 Individual cascade annealing in BCC tungsten: effects of size and spatial distributions of defects *RSC Adv.* **12** 23176–82

[41] Liu L., Gao N., Chen Y., Qiu R., Hu W., Gao F. and Deng H. 2021 Formation mechanism of $\langle\ 111\ \rangle$ interstitial dislocation loops from irradiation-induced C15 clusters in tungsten *Phys. Rev. Mater.* **5** 093605

[42] Liu L., Qiu R., Chen Y., Jiang M., Gao N., Huang B., Gao F., Hu W. and Deng H. 2023 Displacement cascades database from molecular dynamics simulations in tungsten *J. Nucl. Mater.* **580** 154415

[43] Castin N., Dwivedi P., Messina L., Bakaev A., Terentyev D. and Bonny G. 2020 The effect of rhenium on the diffusion of small interstitial clusters in tungsten *Comput. Mater. Sci.* **177** 109580

[44] Becquart C.S., Domain C., Sarkar U., DeBacker A. and Hou M. 2010 Microstructural evolution of irradiated tungsten: ab initio parameterisation of an OKMC model *J. Nucl. Mater.* **403** 75–88

[45] Gao J., Gaganidze E. and Aktaa J. 2022 Relative population of 1/2 and interstitial loops in alpha-Fe under irradiation: effects of C15 cluster stability and loop one-dimensional movement *Acta Mater.* **233** 117983

[46] Kohnert A.A. and Wirth B.D. 2015 Cluster dynamics models of irradiation damage accumulation in ferritic iron. II. Effects of reaction dimensionality *J. Appl. Phys.* **117** 154306

[47] Ahlgren T., Heinola K., Juslin N. and Kuronen A. 2010 Bond-order potential for point and extended defect simulations in tungsten *J. Appl. Phys.* **107** 033516

[48] Olsson P.A.T. 2009 Semi-empirical atomistic study of point defect properties in BCC transition metals *Comput. Mater. Sci.* **47** 135–45

[49] Fikar J., Schäublin R., Mason D.R. and Nguyen-Manh D. 2018 Nano-sized prismatic vacancy dislocation loops and vacancy clusters in tungsten *Nucl. Mater. Energy* **16** 60–65

[50] Gao J., Gaganidze E. and Aktaa J. 2022 Parameterization on formation free energy of dislocation loops up to 1100 K in bcc iron *J. Nucl. Mater.* **559** 153409

[51] Dudarev S.L., Bullough R. and Derlet P.M. 2008 Effect of the $\alpha - \gamma$ phase transition on the stability of dislocation loops in bcc iron *Phys. Rev. Lett.* **100** 135503

[52] Alexander R., Marinica M.-C., Proville L., Willaime F., Arakawa K., Gilbert M.R. and Dudarev S.L. 2016 *Ab initio* scaling laws for the formation energy of nanosized interstitial defect clusters in iron, tungsten, and vanadium *Phys. Rev. B* **94** 024103

[53] Huang S. and Marian J. 2019 Rates of diffusion controlled reactions for one-dimensionally-moving species in 3D space *Phil. Mag.* **99** 2562–83

[54] Wolfer W.G. 2007 The dislocation bias *J. Comput.-Aided Mater. Des.* **14** 403–17

[55] Marian J., Wirth B.D. and Perlado J.M. 2002 Mechanism of formation and growth of $\langle 100 \rangle$ interstitial loops in ferritic materials *Phys. Rev. Lett.* **88** 255507

[56] Bakaev A., Bonny G., Castin N., Terentyev D. and Bakaev V.A. 2021 Impact of interstitial impurities on the trapping of dislocation loops in tungsten *Sci. Rep.* **11** 12333

[57] Was G.S. 2017 *Fundamentals of Radiation Materials Science* (Springer) (https://doi.org/10.1007/978-1-4939-3438-6)

[58] Bhattacharya A., Meslin E., Henry J., Décamps B. and Barbu A. 2018 Dramatic reduction of void swelling by helium in ion-irradiated high purity α—iron *Mater. Res. Lett.* **6** 372–7

[59] Surh M.P., Sturgeon J.B. and Wolfer W.G. 2008 Void nucleation, growth, and coalescence in irradiated metals *J. Nucl. Mater.* **378** 86–97

[60] Trinkaus H. and Singh B.N. 2003 Helium accumulation in metals during irradiation—where do we stand? *J. Nucl. Mater.* **323** 229–42

[61] Langtangen P. and Wang L. 2015 Odespy software package (available at: https://github.com/hplgit/odespy)

[62] Hindmarsh A.C. 1982 *Toward a Systematized Collection of ODE Solvers* (Lawrence Livermore National Laboratory)

[63] Golubov S.I., Ovcharenko A.M., Barashev A.V. and Singh B.N. 2001 Grouping method for the approximate solution of a kinetic equation describing the evolution of point-defect clusters *Phil. Mag. A* **81** 643–58

[64] Pelowitz D. *et al* 2011 MCNPX 2.7.0 extensions (https://doi.org/10.2172/1058045)

[65] Stankovskiy A., Van den Eynde G. and Fiorito L. 2018 *ALEPH V.2.7, A Monte Carlo Burn-Up Code* (SCK•CEN)

[66] Plompen A.J.M. *et al* 2020 The joint evaluated fission and fusion nuclear data library, JEFF-3.3 *Eur. Phys. J. A* **56** 181

[67] Brown D.A. *et al* 2018 ENDF/B-VIII.0: the 8th major release of the nuclear reaction data library with CIELO-project

cross sections, new standards and thermal scattering data *Nucl. Data Sheets* **148** 1–142

[68] Konobeyev A., Yu,Fischer U., Korovin Yu A. and Simakov S.P. 2017 Evaluation of effective threshold displacement energies and other data required for the calculation of advanced atomic displacement cross-sections *Nucl. Energy Technol.* **3** 169–75

[69] Yin C., Terentyev D., Zhang T., Petrov R.H. and Pardoen T. 2020 Impact of neutron irradiation on the strength and ductility of pure and ZrC reinforced tungsten grades *J. Nucl. Mater.* **537** 152226

[70] Byggmästar J., Granberg F., Sand A.E., Pirttikoski A., Alexander R., Marinica M.-C. and Nordlund K. 2019 Collision cascades overlapping with self-interstitial defect clusters in Fe and W *J. Phys.: Condens. Matter* **31** 245402

[71] Fellman A. and Sand A.E. 2022 Recoil energy dependence of primary radiation damage in tungsten from cascade overlap with voids *J. Nucl. Mater.* **572** 154020

[72] De Backer A., Sand A.E., Nordlund K., Luneville L., Simeone D. and Dudarev S.L. 2016 Subcascade formation and defect cluster size scaling in high-energy collision events in metals *EPL Europhys. Lett.* **115** 26001

[73] Gilbert M.R. and Sublet J.-C. 2018 Differential dpa calculations with SPECTRA-PKA *J. Nucl. Mater.* **504** 101–8

[74] Koning A.J., Rochman D., Sublet J.-Ch., Dzysiuk N., Fleming M. and van der Marck S. 2019 TENDL: Complete Nuclear Data Library for Innovative Nuclear Science and Technology *Nucl. Data Sheets* **155**

[75] Haley J.C., Briggs S.A., Edmondson P.D., Sridharan K., Roberts S.G., Lozano-Perez S. and Field K.G. 2017 Dislocation loop evolution during in-situ ion irradiation of model FeCrAl alloys *Acta Mater.* **136** 390–401

[76] Li Y., Ran G., Liu X., Han Q., Huang X. and Ding Y. 2022 In-situ TEM investigation of dislocation loop reaction and irradiation hardening in $H2^{+}$–He^{+} dual-beam irradiated Mo *J. Mater. Sci. Technol.* **107** 14–25